





18 **Abstract**

19 Changes in land cover and aerosols resulting from urbanization may impact convective clouds  
20 and precipitation. Here we investigate how Houston urbanization can modify sea-breeze induced  
21 convective cloud and precipitation through urban land effect and anthropogenic aerosol effect.  
22 The simulations are carried out with the Chemistry version of the Weather Research and  
23 Forecasting model (WRF-Chem), which is coupled with the spectral-bin microphysics (SBM)  
24 and the multilayer urban model with a building energy model (BEM-BEP). We find that  
25 Houston urbanization (the joint effect of both urban land and anthropogenic aerosols) notably  
26 enhances storm intensity (by  $\sim 15 \text{ m s}^{-1}$  in maximum vertical velocity) and precipitation intensity  
27 (up to 45%), with the anthropogenic aerosol effect more significant than the urban land effect.  
28 Urban land effect modifies convective evolution: speed up the transition from the warm cloud to  
29 mixed-phase cloud thus initiating surface rain earlier but slowing down the convective cell  
30 dissipation, all of which result from urban heating induced stronger sea breeze circulation. The  
31 anthropogenic aerosol effect becomes evident after the cloud evolves into the mixed-phase  
32 cloud, accelerating the development of storm from the mixed-phase cloud to deep cloud by  $\sim 40$   
33 min. Through aerosol-cloud interaction (ACI), aerosols boost convective intensity and  
34 precipitation mainly by activating numerous ultrafine particles at the mixed-phase and deep  
35 cloud stages. This work shows the importance of considering both urban land and anthropogenic  
36 aerosol effects for understanding urbanization effects on convective clouds and precipitation.

37



## 38 **1 Introduction**

39           Urbanization has been a significant change of the earth environment since  
40 industrialization and is expected to further expand during the coming decades (Agli et al., 2004).  
41 Many modeling and observational studies have shown that urbanization can impact weather and  
42 climate (e.g., Shepherd et al., 2010; Ashley et al., 2012).

43           Urbanization could impact storm properties through two major pathways. The first major  
44 pathway is through the changes on land cover types. For urban land, the most typical and  
45 extensively studied effect is the increase of surface temperature compared to the surrounding  
46 rural area, known as the urban heat island (UHI) effect (e.g., Bornstein and Lin, 2000; Shepherd,  
47 2005; Hubbard et al., 2014). Convective storms may be initiated at the UHI convergence zone,  
48 created through a combination of increased temperature and mechanical turbulence resulting  
49 from complex urban surface geometry and roughness (Bornstein and Lin, 2000; Shepherd, 2005,  
50 Hubbard et al., 2014). Urban landscapes impact sensible and latent heat flux, soil moisture, etc.,  
51 affecting thunderstorm initiation (Haberlie et al., 2015) and changing the location and amount of  
52 precipitation compared to pre-urbanization period (Shepherd et al. 2002; Niyogi et al. 2011).

53           The second major pathway of the urbanization impacts is through pollutant aerosols  
54 associated with industrial and population growth in cities. Previous studies have shown that  
55 urban aerosols invigorate precipitation in urban downwind regions through aerosol-cloud  
56 interaction (ACI; Van den Heever and Cotton 2007; Carrió et al. 2010; Fan et al., 2018). A  
57 recent study showed aerosol spatial variability in the Seoul area played an important role in a  
58 torrential rain event (Lee et al., 2018). Many compelling evidences have emerged showing the  
59 joint influences of aerosols and urban land on clouds and precipitation, especially in China where  
60 both effects are strong and complex (Li et al., 2019 and references therein).



61 Majority of the past studies focused on one of the abovementioned pathways. Recently, a  
62 few studies examined the combined effects of both pathways on lightning and precipitation. A  
63 new observational study (Kar and Liou, 2019) indicated that both land and aerosol effects should  
64 be considered to explain the cloud-to-ground lightning enhancements over the urban areas.  
65 Modeling study showed urban land-cover changes increased precipitation over the upstream  
66 region but decreased precipitation over the downstream region, while aerosols had the opposite  
67 effect mainly through the indirect effect (Zhong et al. 2015). A long-period (5 years) modeling  
68 study in the Yangtze River Delta (YRD) region confirmed the opposite effects on precipitation  
69 but aerosol radiative effect was the dominant reason for the reduced convective intensity and  
70 precipitation (Zhong et al. 2017). Sarangi et al. (2018) also showed the enhanced precipitation  
71 over the urban core by the urban land effect and at the downwind region by the aerosol effect,  
72 consistent with Zhong et al (2015). Schmid and Niyogi (2017) showed that urban precipitation  
73 rate enhancement is due to a combination of land heterogeneity induced dynamical lifting effect  
74 and aerosol indirect effects. For coastal cities, studies indicated that anthropogenic aerosol effect  
75 on precipitation may be more important than the urban land effect (Liu and Niyogi et al., 2019,  
76 Ganeshan et al., 2013; Ochoa et al., 2015).

77 Houston is the largest city in the southern United States. It is one of the most polluted  
78 areas in the nation based on the most recent “State of the Air” report by American Lung  
79 Association (<http://www.stateoftheair.org/about/>). The Houston urbanization causes both land  
80 cover change and anthropogenic emission enhancement which has been a fertile region for air  
81 quality studies (i.e., high ozone) (e.g., Chen et al., 2011, Fast et al., 2006). The sea breeze  
82 circulation over the region plays a key role not only in convection and precipitation but also in  
83 local air quality (Fan et al., 2007; Banta et al. 2005, Caicedo et al., 2019). The strength and





84 inland propagation of sea breeze circulation can be influenced by land/sea surface temperature  
85 contrast, land use/land cover, and the prevailing synoptic flow (e.g., Angevine et al., 2006; Bao  
86 et al., 2005; Chen et al., 2011). Chen et al. (2011) indicated that the existence of the Houston city  
87 favored stagnation because the inland penetration of the sea breeze counteracted the prevailing  
88 wind in a case study. On the other hand, Ryu et al. (2016) showed the urban heating of  
89 Baltimore–Washington metropolitan area strengthened the bay breeze thus promoted intense  
90 convection and heavy rainfall. In Shanghai, however, the sea-land breeze has exhibited a  
91 weakening trend over the past 21 years, which was hypothesized to result from the joint  
92 influences of aerosol, UHI, and greenhouse effects (Shen et al., 2019). While sorting out the  
93 various factors is a daunting task especially by means of observation analysis, it is essential to  
94 enhance our understanding of both overall effects by human activity and individual ones for  
95 which much fewer have been done.

96 In this study, we aim at understanding how the changes in Houston land cover and  
97 anthropogenic aerosols as a result of urbanization modify the sea-breeze induced convective  
98 storm and precipitation jointly and respectively. To answer the science question, we employ the  
99 Chemistry version of Weather Research and Forecast (WRF) model coupled with the spectral-  
100 bin microphysics (WRF-Chem-SBM) scheme, a model we previously developed and applied to  
101 warm stratocumulus clouds (Gao et al., 2016), to simulate a deep convective storm case that  
102 occurred over the Houston region and produced heavy precipitation. Sensitivity tests are  
103 performed to look into the joint and respective effects of urban land and anthropogenic aerosol  
104 on storm development and precipitation.



## 105 **2 Case Description, Model, and Analysis Method**

### 106 **2.1 Case description**

107 The deep convective cloud event we simulate in this study occurred on 19-20 June 2013  
108 near Houston, Texas. The case was also selected for the ACPC Model Intercomparison Project  
109 (Rosenfeld et al., 2014; [www.acpcinitiative.org](http://www.acpcinitiative.org)). In another companion study (Zhang et al.,  
110 2020), this case was simulated to study the impact of cloud microphysics parameterizations on  
111 ACI. The isolated weak convective clouds were initiated from the late morning because of a  
112 trailing front. Deep convective cells over Houston and Galveston bay areas developed in the  
113 afternoon with increased solar heating and strengthened sea breeze circulation. A strong  
114 convective cell observed in the Houston city that we focused was initiated at 2145 UTC (local  
115 time 16:45) and developed to its peak precipitation at 2217 UTC.

116 The simulated case was evaluated extensively in aerosol and cloud properties in the  
117 companion paper mentioned above. Here only observations of radar reflectivity and precipitation  
118 are used in the evaluation. The radar reflectivity is obtained from the Next-Generation Weather  
119 Radar (NEXRAD) network at <https://www.ncdc.noaa.gov/data-access/radar-data/nexrad->  
120 products, with a temporal frequency of every ~5 minutes and a spatial resolution of 1 km. The  
121 high-temporal and spatial precipitation data retrieved based on radar reflectivity is used for  
122 simulation evaluation.

### 123 **2.2 Model description and experiment design**

124 The WRF-Chem-SBM model used in this study is based on Gao et al. (2016), with  
125 updates in both WRF-Chem (Grell et al., 2005; Skamarock et al., 2008) and the SBM (Khain et  
126 al., 2004; Fan et al., 2012). The SBM version coupled with WRF-Chem is a fast version with



127 only four sets of 33 bins for representing size distribution of CCN, drop, ice/snow, and  
128 graupel/hail, respectively. It is currently coupled with the four-sector version of the Model for  
129 Simulating Aerosol Interactions and Chemistry (MOSAIC) (Fast et al., 2006; Zaveri et al.,  
130 2008). Compared with the original WRF-Chem model which uses two-moment bulk  
131 microphysics schemes, besides the advancements in cloud microphysical process calculations in  
132 SBM, the aerosol-cloud interaction processes which impact both cloud and aerosol properties are  
133 physically improved. These processes are aerosol activation, resuspension, and in-cloud wet-  
134 removal (Gao et al., 2016). Theoretically both aerosol and cloud processes can be more  
135 realistically simulated compared with the original WRF-Chem, particularly under the conditions  
136 of complicated aerosol compositions and aerosol spatial heterogeneity. This would result in  
137 improved simulations of both ACI and aerosol-radiation interactions (ARI). Following on Gao et  
138 al. (2016) where the model was applied to a warm stratocumulus cloud case, we apply the model  
139 to the deep convective storm case in this study.

140 The dynamic core of WRF-Chem-SBM is the Advanced Research WRF model that is fully  
141 compressible and nonhydrostatic with a terrain-following hydrostatic pressure vertical coordinate  
142 (Skamarock et al., 2008). The grid staggering is the Arakawa C-grid. The model uses the Runge-  
143 Kutta 3rd order time integration schemes, and the 3rd and 5th order advection schemes are selected  
144 for the vertical and horizontal directions, respectively. The positive definite option is employed  
145 for advection of moist and scalar variables.

146 The model domains are shown in Fig. 1. Two nested domains have horizontal grid  
147 spacings of 2 and 0.5 km, respectively, with 51 vertical levels up to 50 hPa. Domain 1  
148 simulations are run with WRF-Chem using Morrison double-moment scheme (Morrison et al.,  
149 2005) to produce realistic aerosol fields for Domain 2 simulations. Two simulations were run



150 over Domain 1 with anthropogenic emissions turned on and off, respectively, starting from 0000  
151 UTC 14 Jun and ending at 1200 UTC 20 June with about 5 days for chemical spin up. The  
152 chemical lateral boundary and initial conditions for Domain 1 simulations were from a quasi-  
153 global WRF-Chem simulations at 1-degree grid spacing, and meteorological lateral boundary  
154 and initial conditions were created from MERRA-2 (Gelaro et al., 2017). Domain 2 simulations  
155 uses WRF-Chem-SBM, driven with the initial and lateral boundary aerosol and chemical fields  
156 from Domain 1 outputs, but the initial and lateral boundary conditions for meteorological fields  
157 are from MERRA-2. The reason for not using the meteorological fields from Domain 1  
158 simulations is that the meteorological fields are different between the simulations with and  
159 without anthropogenic emissions. To use the same meteorological fields that do not much  
160 account for small-scale urban land and aerosol effects to drive all simulations carried out over  
161 Domain 2, MERRA-2 data are used. Domain 2 simulations are initiated at 0600 UTC 19 June (~  
162 5 days later from the initial time of Domain 1 simulations) and run for 30 hours. The modeled  
163 dynamic time step was 6 s for Domain 1 simulations and 3 s for Domain 2 simulations.

164 For all simulations over both domains, the anthropogenic emission was from NEI-2011  
165 emissions. The biogenic emission came from the Model of Emissions of Gases and Aerosols  
166 from Nature (MEGAN) product (Guenther et al., 2006). The biomass burning emission was from  
167 the Fire Inventory from NCAR (FINN) model (Wiedinmyer et al., 2011).

168 The baseline simulation over Domain 2 uses the initial and boundary chemical and  
169 aerosol conditions from the Domain 1 simulation with anthropogenic emissions turned on. This  
170 simulation uses all available emissions as abovementioned including anthropogenic emissions. It  
171 is the same simulation as “SBM\_anth” in Zhang et al. (2020). Here we renamed it as  
172 “LandAero”, in which the effects of urban land and anthropogenic aerosols are considered (Fig.



173 2a, c). Based on LandAero, sensitivity tests are conducted to investigate the combined and  
174 individual effects of urban land and anthropogenic aerosols. No\_Aero is the simulation based on  
175 LandAero, except that anthropogenic emissions are turned off and the initial and boundary  
176 chemical and aerosol conditions are from the Domain 1 simulation without anthropogenic  
177 aerosols considered (Fig. 2b). No\_Land is also based on LandAero, except the Houston urban  
178 land is replaced by the surrounding cropland and pasture (Fig. 2d). The aerosols used in  
179 No\_Land include the anthropogenic sources (Fig. 2a), which is analogous to the scenario of  
180 downwind a big city (i.e., rural area with pollution particles transported from city). We also run a  
181 simulation with both the urban land cover replaced by the surrounding cropland and the  
182 anthropogenic aerosols excluded (Fig. 2b, d), which is referred to as “No\_LandAero”. That is,  
183 both effects of urban land and anthropogenic aerosol are not considered in this simulation. By  
184 comparing LandAero with No\_LandAero, the joint effect of urban land and anthropogenic  
185 aerosols can be obtained. The individual urban land and anthropogenic aerosol effect can be  
186 obtained by comparing LandAero with No\_Land and LandAero with No\_Aero, respectively.

187         The simulated aerosol and CCN properties are evaluated with observations in Zhang et al.  
188 (2020), which shows that the model captures aerosol mass and CCN number concentrations  
189 reasonably well. Aerosol number concentration is not evaluated because the measurements are  
190 not available at the Texas Commission for Environmental Quality (TCEQ) sites. A snapshot of  
191 simulated aerosol number concentrations in LandAero and No\_Aero at the time of 6 hours before  
192 the initiation of the Houston cell is shown in Fig. 2a-b. Houston anthropogenic emissions  
193 produce about 10 times more aerosol concentrations over the Houston area than those in Gulf of  
194 Mexico and ~ 5 times than those in the rural area shown in Fig. 2a. The background aerosol  
195 concentrations are relatively low (around  $250 \text{ cm}^{-3}$ ) in this region. Aerosols over the Houston



196 urban area are mainly contributed by organic aerosols, which are highly related with the oil  
197 refinery industry and ship channel emissions. The aerosol compositions are mainly sulfate in the  
198 rural area and sea salt over the Gulf of Mexico in our simulations. Therefore, aerosol properties  
199 are extremely heterogenous in this region. Fig. 3 shows the mean aerosol size distributions from  
200 the three area as marked up in Fig. 2a in LandAero. In the Houston area, majority of aerosols  
201 (75%) have a size (diameter) smaller than 100 nm, and 51% of the aerosols is ultrafine aerosol  
202 particles (smaller than 60 nm). Those small particles are substantially reduced in the rural area  
203 and the Gulf of Mexico (Fig. 3).

204 To see how the land cover type change affects temperature, Fig. 4 shows the differences  
205 of 2-m temperature and surface sensible heat fluxes between LandAero and No\_Land at 1600  
206 UTC when sea breeze begins to show differences. The urban land increases near-surface  
207 temperature over Houston and its downwind area by about 1-2 °C (Fig. 4a), corresponding to the  
208 increase of surface sensible heat fluxes (Fig. 4b). More information about the temporal evolution  
209 and vertical distribution of the urban heating will be discussed in the result section.

### 210 **2.3 Analysis Method**

211 To quantify the convective cell properties occurring over Houston, we employ the Multi  
212 Cell Identification and Tracking (MCIT) Algorithm from Hu et al. (2019a) to track the  
213 convective storms. The MCIT is a watershed-based algorithm and shows better tracking  
214 capabilities compared with traditional centroid based tracking algorithms. The MCIT identifies  
215 cells by local maxima of vertically integrated liquid (VIL) based on watershed principles and  
216 performs tracking of multiple cells base on maximum common VIL between the consecutive  
217 scans. In this way, convective storm life cycle from initiation to dissipation can be better tracked  
218 than the traditional methods as detailed in Hu et al. (2019a).



219 To apply the algorithm to both model simulation and NEXRAD observations  
220 consistently in this study, we calculated liquid water path (LWP), a variable of model output  
221 accounting for the column integrated liquid to replace VIL in MCIT for model simulation. We  
222 track local maxima of LWP by identifying the two cells in consecutive radar scans that have  
223 maximum common LWP. A cell is identified and tracked when the local maxima LWP exceeds  
224  $50 \text{ g m}^{-2}$ . This value is selected because it allows us to start recognizing the deep convective cell  
225 by filtering a lot of shallow clouds surrounded it. The storm area of the tracked cell is defined as  
226 the grid area with  $\text{LWP} > 50 \text{ g m}^{-2}$ .

227 To examine sea breeze circulation over the Houston region, the sea breeze wind intensity  
228 at a specific time is calculated by averaging the horizontal wind speeds below 1-km altitude  
229 along the black line UO in Fig. 4a. The cross section of the winds along this line is also analyzed  
230 in the result section.

## 231 **3 Results**

### 232 **3.1 Radar reflectivity, precipitation, and convective intensity**

233 We first discuss the evaluation of the baseline simulation LandAero first. The simulation  
234 is comprehensively evaluated in Zhang et al. (2020). Here the comparisons with observed radar  
235 reflectivity and precipitation are included. The composite radar reflectivity at the time of the  
236 peak reflectivity of the storm in Houston shows that LandAero captures the convective cell in  
237 Houston, with the maximal radar reflectivity of 58 dBZ, very close to the observed 57 dBZ (Fig.  
238 5a, b). The modeled convective cell in LandAero has a larger size compared with the radar  
239 observations. The contoured frequency by altitude diagram (CFAD) over the major storm period  
240 (1800 UTC 19 Jun to 0000 UTC 20 Jun) shows that the model overestimates the frequencies of



241 moderate reflectivity (i.e., 15-35 dBZ) over the entire vertical profile (Fig. 6a-b), but captures the  
242 occurrence frequencies of high reflectivity (larger than 45 dBZ) reasonably well. The magnitude  
243 of the surface rain rate averaged over the study area defined by the red box in Fig. 5 from  
244 LandAero agrees with the retrieved value from the NEXRAD reflectivity, with a peak time about  
245 40 min earlier than the observation (Fig. 7a). The probability density function (PDF) of rain rates  
246 shows that LandAero reproduces the occurrence frequencies of low and mediate rain rates well  
247 (left two columns in Fig. 7b) and overestimates the occurrence frequencies of high rain rates ( $>$   
248  $10 \text{ mm h}^{-1}$ ; right two columns in Fig. 7b). The accumulated precipitation over the time period  
249 shown in Fig. 7a is about 7.2 mm from LandAero and 5.5 mm from observations, with a model  
250 overestimated of  $\sim 30\%$  because of the overestimation of occurrences of high rain rates and  
251 longer precipitation period.

252 Without Houston urbanization (i.e., both effects of urban land and anthropogenic aerosol  
253 are removed), the Houston convective cell is a lot smaller in area and has reflectivity values of  $\sim$   
254 7 dBZ lower in general compared with LandAero and the NEXRAD observation (Fig. 5c vs. 5a-  
255 b). There is almost no radar reflectivity larger than 50 dBZ in No\_LandAero (Fig. 6c), in  
256 contrast with the significant occurrences of reflectivity larger than 50 dBZ in LandAero and the  
257 NEXRAD observation. Those differences are more clearly shown in Fig. 6f. The peak surface  
258 rain rate in No\_LandAero is reduced by  $\sim 45\%$  compared with LandAero and observations (Fig.  
259 7a; black vs. red line), with the occurrences of large rain rates ( $> 15 \text{ mm h}^{-1}$ ) reduced by nearly  
260 an order of magnitude (Fig. 7b). In terms of updraft intensity, the CFAD plots in Fig. 8a-b show  
261 that there is extremely low or no occurrence for updraft velocity larger than  $15 \text{ m s}^{-1}$  in  
262 No\_LandAero, while the occurrences of  $30 \text{ m s}^{-1}$  still exist in LandAero. There are less  
263 occurrences of weak updraft velocities and more occurrences of relatively strong updraft





264 velocities over the vertical profile (Fig. 8e). These results indicate the urbanization (i.e., the joint  
265 urban land and aerosol effects) drastically enhances the convective intensity and precipitation.

266 Now let's look at the individual effect from the Houston urban land and anthropogenic  
267 aerosols. Fig. 5 shows that the urban land effect enlarges the storm area (Fig. 5d vs. 5b) but the  
268 aerosol effect is more significant (Fig. 5e vs. 5b). The CFAD of radar reflectivity in Fig. 6 also  
269 shows that changes of the PDF by the urban land effect is notably smaller than the anthropogenic  
270 aerosol effect. For the occurrence frequencies of high reflectivity larger than 48 dBZ, the change  
271 is mainly from the anthropogenic aerosol effect (Fig. 6f-h).

272 For precipitation, we do not see an important effect of urban land on the magnitudes of  
273 precipitation rate and the PDF of rain rate (Fig. 7a-b; No\_Land vs LandAero). The accumulated  
274 rain is about 6.9 mm, which is also not much different from 7.2 mm in LandAero. In contrary,  
275 the anthropogenic aerosol effect increases the peak rate by ~ 30%. The frequency of large rain  
276 rates ( $> 15 \text{ mm h}^{-1}$ ) is increased by about 5 times (Fig. 7b; No\_Aero vs LandAero). The joint  
277 effect of both urban land and aerosol increases the accumulated rain by ~ 26%, the peak rain  
278 rates by 45%, and the frequency of large rain rates by an order of magnitudes (from  
279 No\_LandAero to LandAero), suggesting the interactions between the two factors amplify the  
280 effect on precipitation, particularly on the large rain rates. Although the Houston urban land  
281 alone does not much affect the magnitude of precipitation, the initial time of the rain is advanced  
282 by ~ 30 min from No\_Land to LandAero (Fig. 7a), indicating that the urban land effect speeds  
283 up the rain formation. Aerosol effect delays the initial and peak rain by ~ 10 min (from No\_Aero  
284 to LandAero). This will be further discussed in Section 3.2 on convective evolution.

285 On convective intensity, the large increases in occurrence frequencies of the updraft  
286 speeds greater than  $10 \text{ m s}^{-1}$  in the upper-levels by the joint effect is mainly contributed by the



287 anthropogenic aerosol effect (Fig. 8e, g). Below 6 km, both the urban land and aerosol effects  
288 play evident roles in increasing the occurrences of relatively large updraft speeds (Fig. 8e-g). The  
289 larger anthropogenic aerosol effect is also clearly seen from the occurrences of maximal vertical  
290 velocity:  $\sim 30 \text{ m s}^{-1}$  in LandAero, while only  $\sim 19 \text{ m s}^{-1}$  in No\_Aero when the anthropogenic  
291 aerosol effect is removed, whereas the value is  $27 \text{ m s}^{-1}$  in No\_Land when the urban land effect  
292 is turned off (Fig. 8a, c-d). The large effect of anthropogenic aerosols on convective intensity  
293 supports the significant aerosol effects on large precipitation rates as shown in Fig. 7. With both  
294 effects removed (No\_LandAero), there are almost 100% reduction for the vertical velocity  
295 greater than  $\sim 15 \text{ m s}^{-1}$ , showing a quite strong enhancement of convective intensity as a result of  
296 urbanization, mainly through the anthropogenic aerosol effects.

### 297 3.2 Convective evolution

298 The urban land effect initiates surface rain about 30 minutes earlier as discussed above,  
299 suggesting that the convective cloud development is affected when urban land effect is  
300 considered. We examine the convective evolution for the cell over Houston using the cell-  
301 tracking method described in Section 2. The time evolution of the tracked cell properties is  
302 shown in Fig. 9a-b. Clearly, the urban land effect enhances the reflectivity and area for the  
303 tracked cell over the lifetime (from the black dashed line to black solid line), and it also  
304 accelerates the development to the peak reflectivity but slows down the dissipation after the peak  
305 radar reflectivity is reached (Fig. 9a-b). The anthropogenic aerosols also enhance the convective  
306 cell reflectivity and area throughout the cell lifecycle (from the black dotted line to black solid  
307 line), with a much larger effect compared with the urban land effect. The anthropogenic aerosol  
308 effect does not affect the timing of peak reflectivity (dotted vs. solid black in Fig. 9a-b). The  
309 overall reflectivity and cell area properties are shown in Fig. 9c-d, which presents a consistent



310 story as Fig. 9a-b. The baseline simulation LandAero tends to overestimate the frequency of big  
311 cell sizes (200-300 km<sup>2</sup>) and underpredict the frequency of small cell size (Fig. 9d). Since  
312 LandAero predicts a similar rain intensity and rain rate PDF as observations as discussed above,  
313 this means that a larger storm cell than observations are needed to predict a similar precipitation  
314 intensity as observations. For this reason, No\_LandAero which predicts much smaller cell size  
315 agrees better with the observations compared with the other simulations purely based on cell size  
316 (Fig. 9b, d). However, as discussed above, other metrics such as peak precipitation rate and PDF  
317 do not support it. It also should be noted that radar reflectivity in model calculation has a large  
318 uncertainty and the model's overestimation can be partly the result of crude Rayleigh scattering  
319 assumptions applied to the model fields. The model overestimation of radar reflectivity has been  
320 commonly found in previous studies at cloud resolving scales (Varble et al. 2011; 2014, Fan et  
321 al., 2015; 2017).

322         Since the small and numerous shallow cumulus clouds are difficult to be tracked with cell  
323 tracking algorithm and they are excluded from the above tracking, to examine how the  
324 convective storm evolves from the initial shallow cumulus period, we chose the red box shown  
325 in Fig. 5 which contains the Houston cell as the study area. Since the convective storm does not  
326 spatially move much with time in this study, this is a valid way to look at the temporal evolution.  
327 Fig. 10 shows the temporal evolution of the maximal total water content (TWC; color contours)  
328 at each level and the maximal vertical velocity in the study area (black line). The convective  
329 storm has three distinct periods: warm cloud, mixed-phase cloud, and deep cloud. The mixed-  
330 phase and deep cloud are defined with a cloud top temperature (cloud top is defined with TWC >  
331 0.01 g kg<sup>-1</sup> at the topmost level) between 0 and -40 °C and below -40 °C, respectively. The purple



332 and black dashed lines in Fig. 10 mark the initiation of mixed-phase and deep clouds,  
333 respectively.

334 As we can see, there is a relatively long warm cloud period for this case (Fig. 10a). With  
335 both urban land and anthropogenic aerosol effects removed, the cloud development from the  
336 warm cloud to mixed-phase cloud is delayed by  $\sim 30$  min (Fig. 10d vs. 10a), so is the  
337 development from the mixed-phase cloud to deep cloud. Compared Fig. 10a with 10b and 10c,  
338 we see that it is mainly the urban land effect that enhances the development of warm cloud to the  
339 mixed-phase cloud by nearly 30 min, while aerosol effect does not affect it (Fig. 10a vs. 10c).  
340 However, it is mainly the aerosol effect that accelerates the development from the mixed-phase  
341 cloud to deep cloud by about 35 min. In the case of the urban land effect removed (i.e.,  
342 No\_Land; Fig. 10b), the anthropogenic aerosol effect makes the duration of the mixed-phase  
343 cloud very short - about 35 mins shorter relative to LandAero in which both effects are  
344 considered and 75 min shorter relative to No\_Aero in which aerosol effect is removed but the  
345 urban land effect is considered. This is due to aerosol invigoration effect in the mixed-phase  
346 cloud stage which will be elaborated later.

347 Accompanying with the faster development of warm cloud to mixed-phase cloud by the  
348 urban land effect is the stronger updraft speeds in the warm cloud stage (shown from the  
349 maximal updraft velocity in Fig. 10 and the mean of the top 25<sup>th</sup> percentile updraft speeds in Fig.  
350 11a). Similarly, for the simulations with the aerosol effect considered (i.e., LandAero and  
351 No\_Land), the convection is stronger in the mixed-phase cloud stage (Fig. 11b), which  
352 accelerates the development into the deep cloud.

353 Now the questions are: (1) how does the urban land effect enhance convective intensity at  
354 the warm cloud stage and speeds up the cloud development from the warm to mixed-phase



355 cloud, but slows down the storm dissipation? (2) how do the anthropogenic aerosols increase  
356 convective intensity at the mixed-phase cloud stage and accelerate the development of mixed-  
357 phase into deep cloud?

358 For Question (1), Fig. 10a and Fig. 12a show that the development of the warm cloud to  
359 mixed-phase cloud occurs when the sea breeze circulation reaches its strongest. Also, the  
360 development corresponds to the fastest and largest increase of sea breeze intensity by the urban  
361 land effect (Fig. 12a). Anthropogenic aerosol does not seem to affect sea breeze circulation. The  
362 enhanced sea breeze circulation in the simulations with the urban land effect considered (i.e.,  
363 LandAero and No\_Aero) compared with No\_Land and No\_LandAero corresponds to the  
364 increases of surface sensible heat flux and air temperature at low levels (Fig. 12b, d), which is  
365 so-called “urban heat island”. The urban heating effect on temperature is significant up to 0.8-km  
366 altitude at its strongest time that also corresponds to strongest sea breeze time (Fig. 13b). The  
367 urban heating enhances convergence in Houston and at the same time increases the temperature  
368 differences between Houston and Gulf of Mexico, both of which would contribute to a stronger  
369 sea breeze circulation. Past studies showed that urban roughness could also enhance low-level  
370 convergence (e.g., Niyogi et al., 2006). However, majority of the studies indicated that increased  
371 surface sensible heat flux is the main reason for the enhanced convergence (Liu and Niyogi,  
372 2019; Shimadera et al., 2015).

373 The stronger sea breeze circulation transports more water vapor to Houston (Fig. 14). At  
374 the time 1930 UTC when the sea breeze is strongest and the enhancement is the largest (Fig.  
375 12a), as well as the temperature contrast between the Houston urban area and Gulf of Mexico is  
376 the largest (Fig. 13b), the low-level moisture in the urban area is clearly higher in LandAero  
377 compared with No\_Land (Fig. 14b, color contour), which would help enhance convection. As a



378 result, the updraft speed of the Houston convective cell is much larger in LandAero compared  
379 with No\_Land (Fig. 14b, contoured line). The stronger convection continues even when sea  
380 breeze dissipates (Fig. 14c) because the heating effect in the urban area extends to the nighttime  
381 until 2300 UTC (local time 18:00; Fig. 12c-d and 13c. This explains the slower dissipation of the  
382 tracked Houston cell by the urban land effect as shown in Fig. 9a-b. In a word, the urban heating  
383 along with the strengthened sea breeze circulation induced by the urban heating enhances  
384 convection at the warm cloud stage and speeds up the development from the warm to mixed-  
385 phase cloud, and the temporally-extended urban heating effect leads to a slower dissipation of  
386 the convective cell.

387 For Question (2), which is about how anthropogenic aerosols increase convective  
388 intensity at the mixed-phase cloud stage and accelerate the development of mixed-phase into  
389 deep cloud, Fig. 11b shows the anthropogenic aerosol effect on updraft speeds becomes notable  
390 at the mixed-phase cloud stage, the effect is doubled compared with the urban land effect at the  
391 mixed-phase regime (6-9 km altitudes). This corresponds to the increased net buoyancy (Fig.  
392 15a, black lines) at those levels from No\_Aero to LandAero, which is mainly because of the  
393 increased thermal buoyancy since condensate loading effect is small (Fig. 15a) as a result of  
394 enhanced condensational heating (Fig. 15c, blue lines). The condensational heating increase is  
395 most significant at 3-5 km and 6-9 km altitudes, corresponding to notably increased secondary  
396 droplet nucleation of small aerosol particles which are not able to be activated at cloud base (Fig.  
397 15e). In this case, aerosols with diameter smaller than 80 nm but larger than 39 nm (the smallest  
398 size in the 4-sectional MOSAIC), which account for about two third of the total simulated  
399 aerosols, are not activated around cloud bases. All of them can be activated in the strong updrafts  
400 (Fan et al., 2018). This strong secondary nucleation leads to increased droplet number and mass



401 by the anthropogenic aerosol effects (from No\_Aero to LandAero; Fig. 16a, c). To recap, the  
402 anthropogenic aerosols enhance updraft velocity at the mixed-phase cloud stage mainly through  
403 enhanced condensation heating (i. e., “warm-phase invigoration”), as a result of nucleating small  
404 aerosol particles below 60 nm which are transported to higher-levels. This mechanism has been  
405 well documented previously (Fan et al., 2007, 2013, 2018; Sheffield et al., 2015; Lebo, 2018).  
406 Thus, the stronger convection speeds up the development of mixed-phase into deep cloud from  
407 No\_Aero to LandAero. For the same reason, the similar acceleration is seen in No\_Land  
408 compared with No\_Aero and No\_LandAero because the anthropogenic aerosol effect is  
409 considered in No\_Land.

410 At the deep cloud stage, the anthropogenic aerosol effect becomes more significant  
411 compared with that in the mixed-phase cloud stage (Fig. 11c vs. 11b), particularly at the low-  
412 levels. We can still see the enhancement of convective intensity by the urban land effect  
413 although the sea breeze difference is relatively smaller at this stage as explained above. The  
414 larger aerosol effect at the deep cloud stage compared with the mixed-phase cloud stage is  
415 because the secondary droplet nucleation above cloud base becomes larger (Fig. 15f). More  
416 aerosols get activated is the result of higher supersaturation since (a) updrafts are stronger than  
417 the mixed-phase cloud stage and (b) more rain forms and removes droplet surface area for  
418 condensation (Fan et. al., 2018). As a result, the latent heating from condensation and then the  
419 thermal buoyancy is increased in a larger magnitude (Fig. 15b, d), thus a larger aerosol impact is  
420 seen at the deep cloud stage. The invigorated deep convection has up to 2 times more ice particle  
421 number concentration and 30% larger ice particle mass mixing ratio (Fig. 16b, d), with the  
422 maximal cloud top height increased by ~ 1 km. The enhanced ice number and mass  
423 concentrations also partially result from freezing of more droplets that are being transported from



424 low levels (Rosenfeld et al., 2008), as suggested from the increased latent heating associated  
425 with the ice phase processes (Fig. 15d). It is obvious that this is not the major mechanism for the  
426 large aerosol effects on convective intensity in this case.

427 Note that both ACI and ARI are considered in the aerosol effects we discussed above,  
428 and the results above suggest ACI plays a key role in invigorating convection. To confirm that,  
429 we conducted two additional sensitivity tests by turning off ARI based on LandAero and  
430 No\_Aero, referred to as LandAero\_ACI and No\_Aero\_ACI, respectively. The differences in  
431 precipitation and convective intensity between LandAero\_ACI and No\_Aero\_ACI (i.e., ACI  
432 effect) are only slightly smaller than the differences between LandAero and No\_Aero (i.e., the  
433 total aerosol effect). This confirms that ACI is the major factor responsible for the convective  
434 invigoration and precipitation enhancement by aerosols.

#### 435 **4 Conclusions and discussion**

436 We have investigated the Houston urbanization effects on convective evolution,  
437 convective intensity, and precipitation of a sea-breeze induced convective storm using the WRF-  
438 Chem coupled with SBM and the BEM-BEP urban canopy model. The baseline simulation with  
439 the urbanization effects considered was extensively evaluated in Zhang et al. (2020) in aerosol  
440 and CCN, surface meteorological measurements, reflectivity and precipitation and in this study  
441 in Houston cell reflectivity and precipitation. The simulated convective storm in Houston was  
442 shown to be consistent with the observed maximal radar reflectivity and peak precipitation  
443 intensity and PDF, despite the peak precipitation time was about ~40 min earlier. The  
444 accumulated rain is overestimated by the baseline simulation due to the longer rain period.

445 Model sensitivity tests were carried out to examine the joint and respective effects of  
446 urban land and anthropogenic aerosols as a result of Houston urbanization on convective





447 evolution and precipitation. We find that the joint effect of Houston urban land and  
448 anthropogenic aerosols enhances the storm intensity (by ~60% in the mean of top 25 percentiles  
449 in deep cloud stage), radar reflectivity (by up to 10 dBZ), peak precipitation rate (by ~ 45%), and  
450 the accumulated rain (by ~ 26%) , with the anthropogenic aerosol effect more significant than the  
451 urban land effect overall. The anthropogenic aerosol effect increases the peak precipitation rate  
452 by ~ 30% and the frequency of large rain rates ( $> 15 \text{ mm h}^{-1}$  by about 5 times). Although urban  
453 land effect alone (under the condition of existence of anthropogenic aerosols) does not impact  
454 the peak precipitation rate and the frequency of large rain rates much, its interaction with aerosol  
455 effects leads to an increase in the peak rain rates by 45% and the frequency of large rain rates by  
456 an order of magnitudes. Therefore, the interactions between the two factors amplify the effect on  
457 precipitation, particularly on the large rain rates, emphasizing the importance of considering both  
458 effects in studying urbanization effects on convective clouds and precipitation.

459         The Houston urban land effect affects the convective evolution, making the initiation of  
460 mixed-phase cloud and surface rain ~30 min earlier because of the strengthened sea breeze  
461 circulation as a result of urban heating. It also slows down the dissipation of convective storm  
462 because the urban heating extends to late afternoon and evening. The aerosol effect from  
463 Houston anthropogenic emissions overall invigorates convection and precipitation, with ACI  
464 dominant. The ACI effect is mainly through enhanced condensation (so-called “warm-phase  
465 invigoration”) by activating numerous small aerosol particles at higher levels above cloud base.  
466 This invigoration is notable starting from the mixed-phase cloud stage and becomes more  
467 significant at the deep cloud stage. The enhanced convective intensity in the mixed-phase cloud  
468 stage by aerosols accelerates the development of convective storm into deep cloud stage by ~ 40  
469 min.



470 This study improves our understanding of how Houston urban land and anthropogenic  
471 aerosols jointly shape thunderstorm in the region. Our findings about the relative importance of  
472 urban land effect versus anthropogenic aerosol effects are consistent with some of previous  
473 studies, which showed that for coastal cities, the anthropogenic aerosol effect on precipitation  
474 was relatively more important than the urban land effect (Liu and Niyogi et al., 2019; Ganeshan  
475 et al., 2013; Ochoa et al., 2015, Hu et al. 2019b). The low background aerosol concentration in  
476 coastal cities is one of the factors responsible for the significant aerosol effect. In Houston,  
477 another factor would be the warm and humid meteorological conditions, in which aerosols were  
478 shown to invigorate convective clouds in many previous studies as reviewed in Tao et al. (2012)  
479 and Fan et al. (2016). The finding that urban land effect enhances sea breeze circulation, which  
480 transports more moisture into the urban area and enhances convection and precipitation, is  
481 consistent with previous studies, such as Ryu et al. (2016) for the Baltimore–Washington  
482 metropolitan area, and You et al. (2019) for the Pearl River delta (PRD) region.

#### 483 **Acknowledgement**

484 This study is supported by the U.S. Department of Energy Office of Science Early Career  
485 Award Program. PNNL is operated for the U.S. Department of Energy (DOE) by Battelle  
486 Memorial Institute under contract DE-AC05-76RL01830. This research used resources of the  
487 PNNL Institutional Computing (PIC), and National Energy Research Scientific Computing  
488 Center (NERSC), a U.S. Department of Energy Office of Science User Facility operated under  
489 Contract No. DE-AC02-05CH11231. The original simulation data will be available through  
490 NERSC data repository after the paper is accepted.

491



492 **Reference**

- 493 Alig, R. J., Kline, J. D., and Lichtenstein, M.: Urbanization on the US landscape: looking ahead in  
494 the 21st century, *Landscape Urban Plan*, 69, 219-234, doi:  
495 10.1016/j.landurbplan.2003.07.004, 2004.
- 496 Angevine, W. M., Tjernstrom, M., and Zagar, M.: Modeling of the coastal boundary layer and  
497 pollutant transport in New England, *J Appl Meteorol Clim*, 45, 137-154, doi:  
498 10.1175/Jam2333.1, 2006.
- 499 Ashley, W. S., Bentley, M. L., and Stallins, J. A.: Urban-induced thunderstorm modification in the  
500 Southeast United States, *Climatic Change*, 113, 481-498, doi: 10.1007/s10584-011-0324-  
501 1, 2012.
- 502 Banta, R. M., Senff, C. J., Nielsen-Gammon, J., Darby, L. S., Ryerson, T. B., Alvarez, R. J.,  
503 Sandberg, S. R., Williams, E. J., and Trainer, M.: A bad air day in Houston, *B Am Meteorol*  
504 *Soc*, 86, 657-669, doi: 10.1175/Bams-86-5-657, 2005.
- 505 Bao, J. W., Michelson, S. A., McKeen, S. A., and Grell, G. A.: Meteorological evaluation of a  
506 weather-chemistry forecasting model using observations from the TEXAS AQS 2000 field  
507 experiment, *J Geophys Res-Atmos*, 110, D21105, doi: 10.1029/2004jd005024, 2005.
- 508 Bornstein, R., and Lin, Q. L.: Urban heat islands and summertime convective thunderstorms in  
509 Atlanta: three case studies, *Atmos Environ*, 34, 507-516, doi: 10.1016/S1352-  
510 2310(99)00374-X, 2000.
- 511 Caicedo, V., Rappenglueck, B., Cuchiara, G., Flynn, J., Ferrare, R., Scarino, A. J., Berkoff, T.,  
512 Senff, C., Langford, A., and Lefer, B.: Bay Breeze and Sea Breeze Circulation Impacts on  
513 the Planetary Boundary Layer and Air Quality From an Observed and Modeled



- 514 DISCOVER-AQ Texas Case Study, *J Geophys Res-Atmos*, 124, 7359-7378, doi:  
515 10.1029/2019jd030523, 2019.
- 516 Carrio, G. G., Cotton, W. R., and Cheng, W. Y. Y.: Urban growth and aerosol effects on convection  
517 over Houston Part I: The August 2000 case, *Atmos Res*, 96, 560-574, doi:  
518 10.1016/j.atmosres.2010.01.005, 2010.
- 519 Chen, F., Miao, S. G., Tewari, M., Bao, J. W., and Kusaka, H.: A numerical study of interactions  
520 between surface forcing and sea breeze circulations and their effects on stagnation in the  
521 greater Houston area, *J Geophys Res-Atmos*, 116, D12105, doi: 10.1029/2010jd015533,  
522 2011.
- 523 Fan, J. W., Zhang, R. Y., Li, G. H., and Tao, W. K.: Effects of aerosols and relative humidity on  
524 cumulus clouds, *J Geophys Res-Atmos*, 112, D14204, doi: 10.1029/2006jd008136, 2007.
- 525 Fan, J. W., Leung, L. R., Li, Z. Q., Morrison, H., Chen, H. B., Zhou, Y. Q., Qian, Y., and Wang,  
526 Y.: Aerosol impacts on clouds and precipitation in eastern China: Results from bin and  
527 bulk microphysics, *J Geophys Res-Atmos*, 117, D00k36, doi: 10.1029/2011jd016537,  
528 2012.
- 529 Fan, J. W., Leung, L. R., Rosenfeld, D., Chen, Q., Li, Z. Q., Zhang, J. Q., and Yan, H. R.:  
530 Microphysical effects determine macrophysical response for aerosol impacts on deep  
531 convective clouds, *P Natl Acad Sci USA*, 110, E4581-E4590, doi:  
532 10.1073/pnas.1316830110, 2013.
- 533 Fan, J. W., Liu, Y. C., Xu, K. M., North, K., Collis, S., Dong, X. Q., Zhang, G. J., Chen, Q., Kollias,  
534 P., and Ghan, S. J.: Improving representation of convective transport for scale-aware  
535 parameterization: 1. Convection and cloud properties simulated with spectral bin and bulk  
536 microphysics, *J Geophys Res-Atmos*, 120, 3485-3509, doi: 10.1002/2014jd022142, 2015.



- 537 Fan, J. W., Wang, Y., Rosenfeld, D., and Liu, X. H.: Review of Aerosol-Cloud Interactions:  
538 Mechanisms, Significance, and Challenges, *J Atmos Sci*, 73, 4221-4252, doi: 10.1175/Jas-  
539 D-16-0037.1, 2016.
- 540 Fan, J. W., Han, B., Varble, A., Morrison, H., North, K., Kollias, P., Chen, B. J., Dong, X. Q.,  
541 Giangrande, S. E., Khain, A., Lin, Y., Mansell, E., Milbrandt, J. A., Stenz, R., Thompson,  
542 G., and Wang, Y.: Cloud-resolving model intercomparison of an MC3E squall line case:  
543 Part I-Convective updrafts, *J Geophys Res-Atmos*, 122, 9351-9378, doi:  
544 10.1002/2017jd026622, 2017.
- 545 Fan, J. W., Rosenfeld, D., Zhang, Y. W., Giangrande, S. E., Li, Z. Q., Machado, L. A. T., Martin,  
546 S. T., Yang, Y., Wang, J., Artaxo, P., Barbosa, H. M. J., Braga, R. C., Comstock, J. M.,  
547 Feng, Z., Gao, W. H., Gomes, H. B., Mei, F., Pohlker, C., Pohlker, M. L., Poschl, U., and  
548 de Souza, R. A. F.: Substantial convection and precipitation enhancements by ultrafine  
549 aerosol particles, *Science*, 359, 411-418, doi: 10.1126/science.aan8461, 2018.
- 550 Fast, J. D., Gustafson, W. I., Easter, R. C., Zaveri, R. A., Barnard, J. C., Chapman, E. G., Grell, G.  
551 A., and Peckham, S. E.: Evolution of ozone, particulates, and aerosol direct radiative  
552 forcing in the vicinity of Houston using a fully coupled meteorology-chemistry-aerosol  
553 model, *J Geophys Res-Atmos*, 111, D21305, doi: 10.1029/2005jd006721, 2006.
- 554 Ganeshan, M., Murtugudde, R., and Imhoff, M. L.: A multi-city analysis of the UHI-influence on  
555 warm season rainfall, *6*, 1-23, doi: 10.1016/j.uclim.2013.09.004, 2013.
- 556 Gao, W. H., Fan, J. W., Easter, R. C., Yang, Q., Zhao, C., and Ghan, S. J.: Coupling spectral-bin  
557 cloud microphysics with the MOSAIC aerosol model in WRF-Chem: Methodology and  
558 results for marine stratocumulus clouds, *J Adv Model Earth Sy*, 8, 1289-1309, doi:  
559 10.1002/2016ms000676, 2016.



- 560 Gelaro, R., McCarty, W., Suarez, M. J., Todling, R., Molod, A., Takacs, L., Randles, C. A.,  
561 Darnenov, A., Bosilovich, M. G., Reichle, R., Wargan, K., Coy, L., Cullather, R., Draper,  
562 C., Akella, S., Buchard, V., Conaty, A., da Silva, A. M., Gu, W., Kim, G. K., Koster, R.,  
563 Lucchesi, R., Merkova, D., Nielsen, J. E., Partyka, G., Pawson, S., Putman, W., Rienecker,  
564 M., Schubert, S. D., Sienkiewicz, M., and Zhao, B.: The Modern-Era Retrospective  
565 Analysis for Research and Applications, Version 2 (MERRA-2), *J Climate*, 30, 5419-5454,  
566 doi: 10.1175/Jcli-D-16-0758.1, 2017.
- 567 Grell, G. A., Peckham, S. E., Schmitz, R., McKeen, S. A., Frost, G., Skamarock, W. C., and Eder,  
568 B.: Fully coupled "online" chemistry within the WRF model, *Atmos Environ*, 39, 6957-  
569 6975, doi: 10.1016/j.atmosenv.2005.04.027, 2005.
- 570 Guenther, A., Karl, T., Harley, P., Wiedinmyer, C., Palmer, P. I., and Geron, C.: Estimates of  
571 global terrestrial isoprene emissions using MEGAN (Model of Emissions of Gases and  
572 Aerosols from Nature), *Atmos Chem Phys*, 6, 3181-3210, doi: 10.5194/acp-6-3181-2006,  
573 2006.
- 574 Haberlie, A. M., Ashley, W. S., and Pingel, T. J.: The effect of urbanisation on the climatology of  
575 thunderstorm initiation, *Q J Roy Meteor Soc*, 141, 663-675, doi: 10.1002/qj.2499, 2015.
- 576 Hu, J. X., Rosenfeld, D., Zrnica, D., Williams, E., Zhang, P. F., Snyder, J. C., Ryzhkov, A.,  
577 Hashimshoni, E., Zhang, R. Y., and Weitz, R.: Tracking and characterization of convective  
578 cells through their maturation into stratiform storm elements using polarimetric radar and  
579 lightning detection, *Atmos Res*, 226, 192-207, doi: 10.1016/j.atmosres.2019.04.015, 2019a.
- 580 Hu, J. X., Rosenfeld, D., Ryzhkov, A., Zrnica, D., Williams, E., Zhang, P. F., Snyder, J. C., Zhang,  
581 R. Y., and Weitz, R.: Polarimetric Radar Convective Cell Tracking Reveals Large



- 582 Sensitivity of Cloud Precipitation and Electrification Properties to CCN, *J Geophys Res-*  
583 *Atmos*, 124, 12194-12205, doi: 10.1029/2019jd030857, 2019b.
- 584 Hu, J. X., Rosenfeld, D., Zrníc, D., Williams, E., Zhang, P. F., Snyder, J. C., Ryzhkov, A.,  
585 Hashimshoni, E., Zhang, R. Y., and Weitz, R.: Tracking and characterization of convective  
586 cells through their maturation into stratiform storm elements using polarimetric radar and  
587 lightning detection, *Atmos Res*, 226, 192-207, doi: 10.1016/j.atmosres.2019.04.015, 2019b.
- 588 Hubbart, J. A., Kellner, E., Hooper, L., Lupo, A. R., Market, P. S., Guinan, P. E., Stephan, K., Fox,  
589 N. I., and Svoma, B. M.: Localized Climate and Surface Energy Flux Alterations across an  
590 Urban Gradient in the Central US, *Energies*, 7, 1770-1791, doi: 10.3390/en7031770, 2014.
- 591 Kar, S. K., and Liou, Y. A.: Influence of Land Use and Land Cover Change on the Formation of  
592 Local Lightning, *Remote Sens-Basel*, 11, 407, doi: 10.3390/rs11040407, 2019.
- 593 Khain, A., Pokrovsky, A., Pinsky, M., Seifert, A., and Phillips, V.: Simulation of effects of  
594 atmospheric aerosols on deep turbulent convective clouds using a spectral microphysics  
595 mixed-phase cumulus cloud model. Part I: Model description and possible applications, *J*  
596 *Atmos Sci*, 61, 2963-2982, doi: 10.1175/Jas-3350.1, 2004.
- 597 Lebo, Z.: A Numerical Investigation of the Potential Effects of Aerosol-Induced Warming and  
598 Updraft Width and Slope on Updraft Intensity in Deep Convective Clouds, *J Atmos Sci*,  
599 75, 535-554, doi: 10.1175/Jas-D-16-0368.1, 2018.
- 600 Lee, S. S., Kim, B. G., Li, Z. Q., Choi, Y. S., Jung, C. H., Um, J., Mok, J., and Seo, K. H.: Aerosol  
601 as a potential factor to control the increasing torrential rain events in urban areas over the  
602 last decades, *Atmos Chem Phys*, 18, 12531-12550, doi: 10.5194/acp-18-12531-2018, 2018.
- 603 Li, Z. Q., Wang, Y., Guo, J. P., Zhao, C. F., Cribb, M. C., Dong, X. Q., Fan, J. W., Gong, D. Y.,  
604 Huang, J. P., Jiang, M. J., Jiang, Y. Q., Lee, S. S., Li, H., Li, J. M., Liu, J. J., Qian, Y.,



- 605 Rosenfeld, D., Shan, S. Y., Sun, Y. L., Wang, H. J., Xin, J. Y., Yan, X., Yang, X., Yang,  
606 X. Q., Zhang, F., and Zheng, Y. T.: East Asian Study of Tropospheric Aerosols and their  
607 Impact on Regional Clouds, Precipitation, and Climate (EAST-AIR(CPC)), *J Geophys*  
608 *Res-Atmos*, 124, 13026-13054, doi: 10.1029/2019jd030758, 2019.
- 609 Liu, J., and Niyogi, D.: Meta-analysis of urbanization impact on rainfall modification, *Sci Rep-*  
610 *Uk*, 9, 7301, doi: 10.1038/s41598-019-42494-2, 2019.
- 611 Morrison, H., Curry, J. A., and Khvorostyanov, V. I.: A new double-moment microphysics  
612 parameterization for application in cloud and climate models. Part I: Description, *J Atmos*  
613 *Sci*, 62, 1665-1677, doi: 10.1175/Jas3446.1, 2005.
- 614 Niyogi, D., Holt, T., Zhong, S., Pyle, P. C., and Basara, J.: Urban and land surface effects on the  
615 30 July 2003 mesoscale convective system event observed in the southern Great Plains, *J*  
616 *Geophys Res-Atmos*, 111, D19107, doi: 10.1029/2005jd006746, 2006.
- 617 Niyogi, D., Pyle, P., Lei, M., Arya, S. P., Kishtawal, C. M., Shepherd, M., Chen, F., and Wolfe,  
618 B.: Urban Modification of Thunderstorms: An Observational Storm Climatology and  
619 Model Case Study for the Indianapolis Urban Region, *J Appl Meteorol Clim*, 50, 1129-  
620 1144, doi: 10.1175/2010jamc1836.1, 2011.
- 621 Ochoa, C. A., Quintanar, A. I., Raga, G. B., and Baumgardner, D.: Changes in Intense Precipitation  
622 Events in Mexico City, *J Hydrometeorol*, 16, 1804-1820, doi: 10.1175/Jhm-D-14-0081.1,  
623 2015.
- 624 Rosenfeld, D., Lohmann, U., Raga, G. B., O'Dowd, C. D., Kulmala, M., Fuzzi, S., Reissell, A.,  
625 and Andreae, M. O.: Flood or drought: How do aerosols affect precipitation?, *Science*, 321,  
626 1309-1313, doi: 10.1126/science.1160606, 2008.





- 627 Ryu, Y. H., Smith, J. A., Bou-Zeid, E., and Baeck, M. L.: The Influence of Land Surface  
628 Heterogeneities on Heavy Convective Rainfall in the Baltimore-Washington Metropolitan  
629 Area, *Mon Weather Rev*, 144, 553-573, doi: 10.1175/Mwr-D-15-0192.1, 2016.
- 630 Sarangi, C., Tripathi, S. N., Qian, Y., Kumar, S., and Leung, L. R.: Aerosol and Urban Land Use  
631 Effect on Rainfall Around Cities in Indo-Gangetic Basin From Observations and Cloud  
632 Resolving Model Simulations, *J Geophys Res-Atmos*, 123, 3645-3667, doi:  
633 10.1002/2017jd028004, 2018.
- 634 Schmid, P. E., and Niyogi, D.: Modeling Urban Precipitation Modification by Spatially  
635 Heterogeneous Aerosols, *J Appl Meteorol Clim*, 56, 2141-2153, doi: 10.1175/Jamc-D-16-  
636 0320.1, 2017.
- 637 Sheffield, A. M., Saleeby, S. M., and van den Heever, S. C.: Aerosol-induced mechanisms for  
638 cumulus congestus growth, *J Geophys Res-Atmos*, 120, 8941-8952, doi:  
639 10.1002/2015jd023743, 2015.
- 640 Shen, L. X., Zhao, C. F., Ma, Z. S., Li, Z. Q., Li, J. P., and Wang, K. C.: Observed decrease of  
641 summer sea-land breeze in Shanghai from 1994 to 2014 and its association with  
642 urbanization, *Atmos Res*, 227, 198-209, doi: 10.1016/j.atmosres.2019.05.007, 2019.
- 643 Shephard, J. M.: A review of current investigations of urban-induced rainfall and  
644 recommendations for the future, *Earth Interact*, 9, doi: 10.1175/EI156.1, 2005.
- 645 Shepherd, J. M., Pierce, H., and Negri, A. J.: Rainfall modification by major urban areas:  
646 Observations from spaceborne rain radar on the TRMM satellite, *J Appl Meteorol*, 41, 689-  
647 701, doi: 10.1175/1520-0450(2002)041<0689:Rmbmua>2.0.Co;2, 2002.
- 648 Shepherd J.M., J.A. Stallins, M. Jin, T.L. Mote: Urbanization: impacts on clouds, precipitation,  
649 and lightning. Monograph on Urban Ecological Ecosystems. Eds. Jacqueline Peterson and

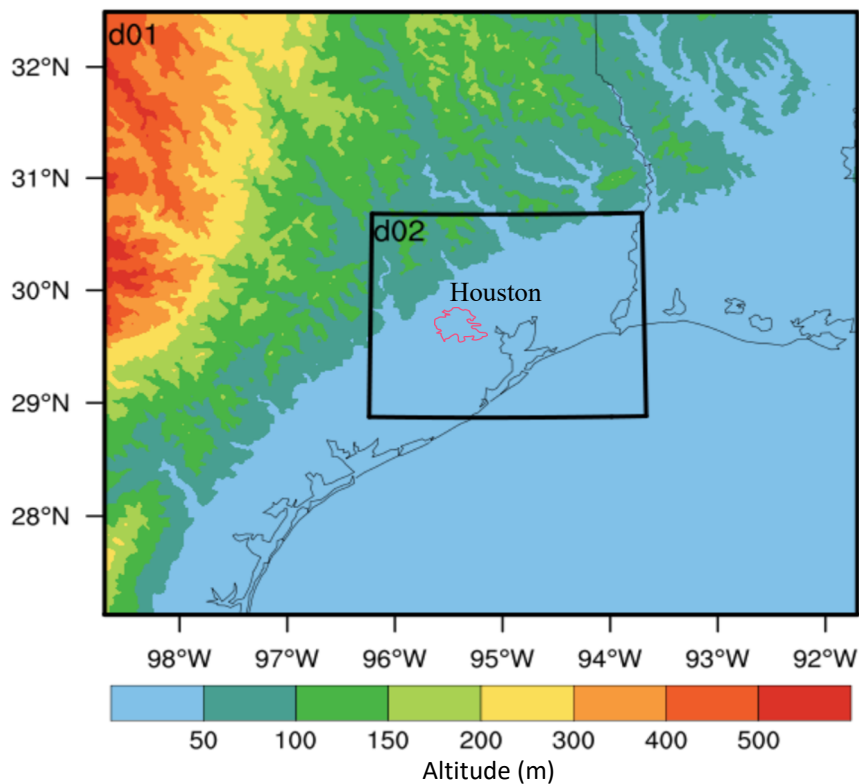


- 650 Astrid Volder. American Society of Agronomy-Crop Science Society of America- Soil  
651 Science Society of America, pp. 354, 2010.
- 652 Shimadera, H., Kondo, A., Shrestha, K. L., Kitaoka, K., and Inoue, Y.: Numerical Evaluation of  
653 the Impact of Urbanization on Summertime Precipitation in Osaka, Japan, *Adv Meteorol*,  
654 379361, doi: 10.1155/2015/379361, 2015.
- 655 Skamarock, W. C., Klemp, J. B., Dudhia, J., Gill, D. O., Barker, D. M., Duda, M., Huang, X. Y.,  
656 Wang, W., and Powers, J. G.: A description of the advanced research WRF version 3,  
657 NCAR, Tech. Note, Mesoscale and Microscale Meteorology Division, National Center for  
658 Atmospheric Research, Boulder, Colorado, USA, 2008.
- 659 Tao, W. K., Chen, J. P., Li, Z. Q., Wang, C., and Zhang, C. D.: Impact of Aerosols on Convective  
660 Clouds and Precipitation, *Rev Geophys*, 50, Rg2001, doi: 10.1029/2011rg000369, 2012.
- 661 Van Den Heever, S. C., and Cotton, W. R.: Urban aerosol impacts on downwind convective storms,  
662 *J Appl Meteorol Clim*, 46, 828-850, doi: 10.1175/Jam2492.1, 2007.
- 663 Varble, A., Fridlind, A. M., Zipser, E. J., Ackerman, A. S., Chaboureau, J. P., Fan, J. W., Hill, A.,  
664 McFarlane, S. A., Pinty, J. P., and Shipway, B.: Evaluation of cloud-resolving model  
665 intercomparison simulations using TWP-ICE observations: Precipitation and cloud  
666 structure, *J Geophys Res-Atmos*, 116, D12206, doi: 10.1029/2010jd015180, 2011.
- 667 Varble, A., Zipser, E. J., Fridlind, A. M., Zhu, P., Ackerman, A. S., Chaboureau, J. P., Fan, J. W.,  
668 Hill, A., Shipway, B., and Williams, C.: Evaluation of cloud-resolving and limited area  
669 model intercomparison simulations using TWP-ICE observations: 2. Precipitation  
670 microphysics, *J Geophys Res-Atmos*, 119, 13919-13945, doi: 10.1002/2013jd021372,  
671 2014.



- 672 Wiedinmyer, C., Akagi, S. K., Yokelson, R. J., Emmons, L. K., Al-Saadi, J. A., Orlando, J. J., and  
673 Soja, A. J.: The Fire INventory from NCAR (FINN): a high resolution global model to  
674 estimate the emissions from open burning, *Geosci Model Dev*, 4, 625-641, doi:  
675 10.5194/gmd-4-625-2011, 2011.
- 676 You, C., Fung, J. C. H., and Tse, W. P.: Response of the Sea Breeze to Urbanization in the Pearl  
677 River Delta Region, *J Appl Meteorol Clim*, 58, 1449-1463, doi: 10.1175/Jamc-D-18-  
678 0081.1, 2019.
- 679 Zaveri, R. A., Easter, R. C., Fast, J. D., and Peters, L. K.: Model for Simulating Aerosol  
680 Interactions and Chemistry (MOSAIC), *J Geophys Res-Atmos*, 113, D13204, doi:  
681 10.1029/2007jd008782, 2008.
- 682 Zhong, S., Qian, Y., Zhao, C., Leung, R., and Yang, X. Q.: A case study of urbanization impact  
683 on summer precipitation in the Greater Beijing Metropolitan Area: Urban heat island  
684 versus aerosol effects, *J Geophys Res-Atmos*, 120, 10903-10914, doi:  
685 10.1002/2015jd023753, 2015.
- 686 Zhong, S., Qian, Y., Zhao, C., Leung, R., Wang, H. L., Yang, B., Fan, J. W., Yan, H. P., Yang, X.  
687 Q., and Liu, D. Q.: Urbanization-induced urban heat island and aerosol effects on climate  
688 extremes in the Yangtze River Delta region of China, *Atmos Chem Phys*, 17, 5439-5457,  
689 doi: 10.5194/acp-17-5439-2017, 2017.
- 690 Zhang Y., Fan J., Li Z., and Rosenfeld D.: Impacts of Cloud Microphysics Parameterizations on  
691 Simulated Aerosol-Cloud-Interactions for Deep Convective Clouds over Houston, *Atmos.*  
692 *Chem. Phys. Discuss.*, <https://doi.org/10.5194/acp-2020-372>, in review, 2020.
- 693  
694

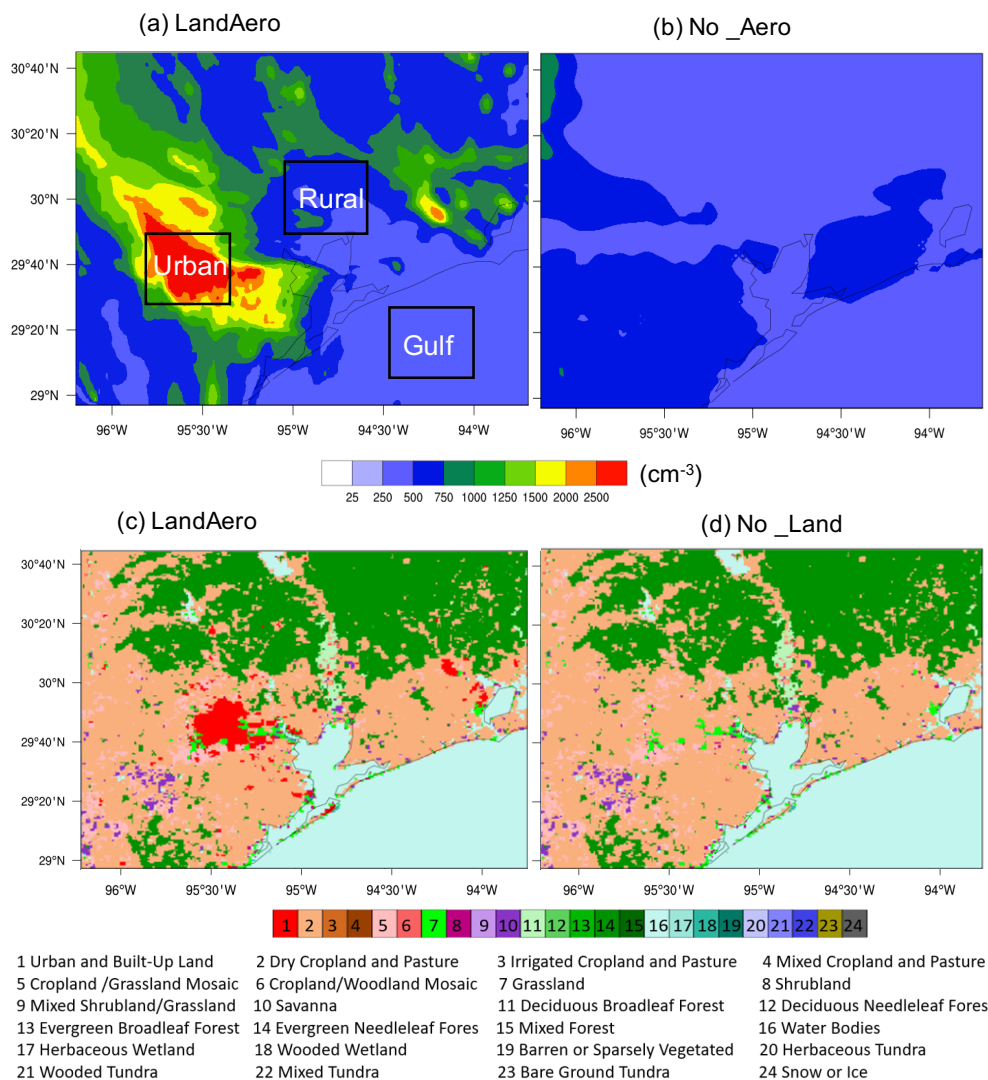




696

697 **Figure 1** The model domain setup. Domain 1 (d01) and Domain 2 (d02) are marked with black  
698 boxes. Terrain heights (m) are in color contours. Houston urban area is denoted by pink  
699 contoured line.

700



701

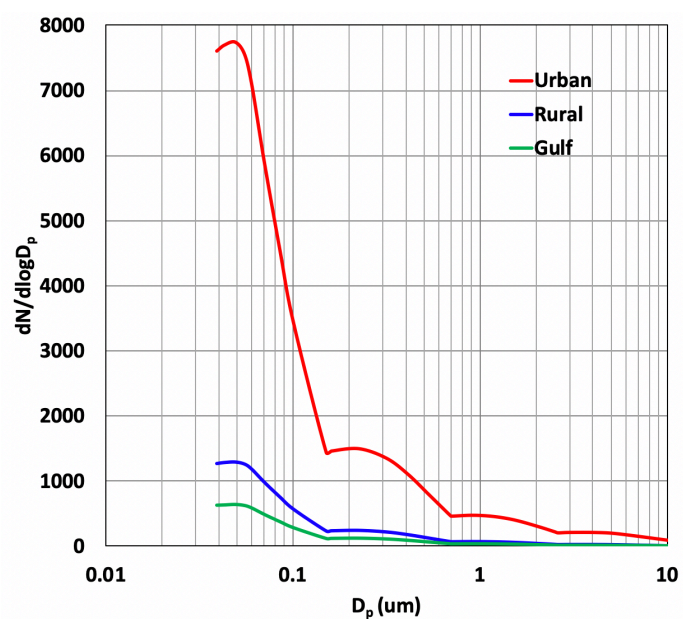
702

703

704

705

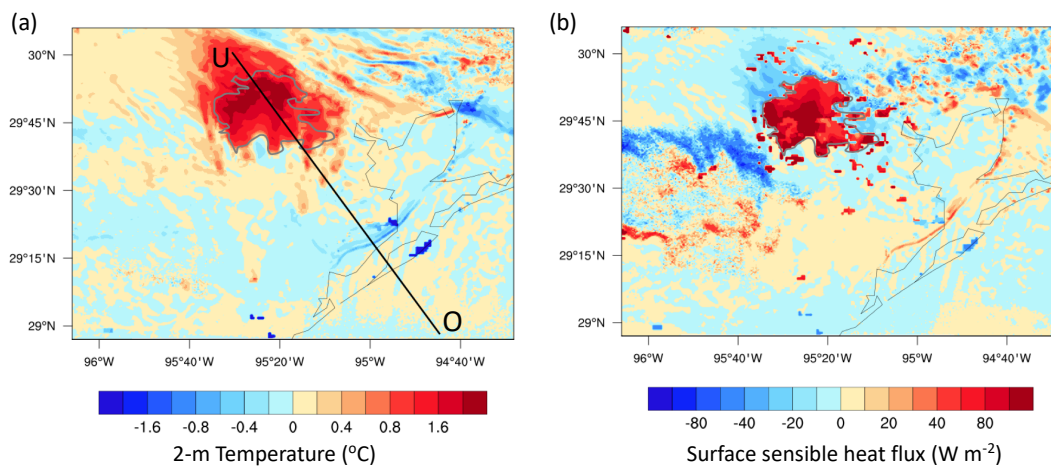
**Figure 2** Aerosol number concentration (cm<sup>-3</sup>) from (a) LandAero (with anthropogenic emission) and (b) No\_Aero (with anthropogenic emission turned off) at 1200 UTC, 19 Jun 2016 (6-hr before the convection initiation), and land cover types in (c) LandAero and (d) No\_Land.



706

707 **Figure 3** Aerosol size distribution over the Urban, Rural, and Gulf of Mexico as marked by three  
708 black boxes in Figure 2a from LandAero at 1200 UTC, 19 Jun 2016.

709



710

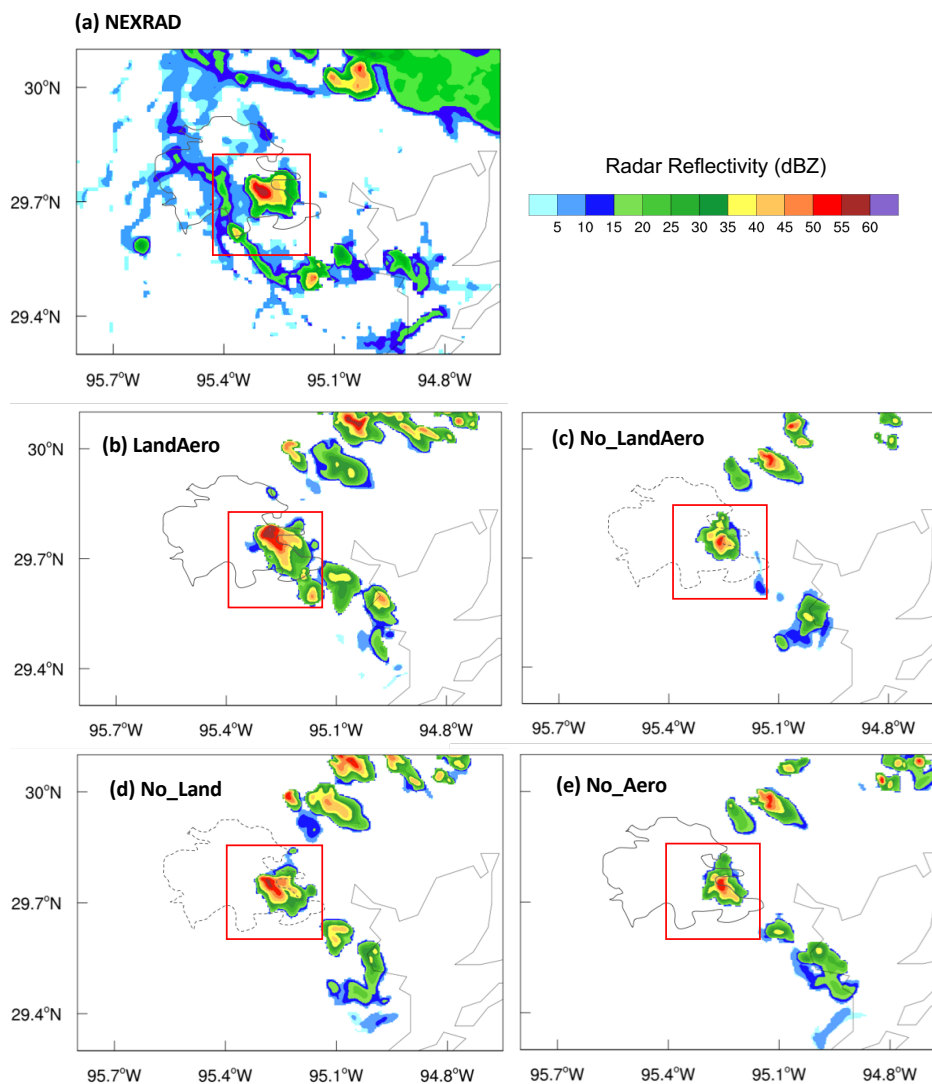
711 **Figure 4** Differences of (a) 2-m temperature ( $^{\circ}\text{C}$ ) and (b) surface sensible heat flux ( $\text{W m}^{-2}$ )

712 between LandAero and No\_Land at 1600 UTC 19 Jun 2013. Line UO is where cross section of

713 sea breeze circulation is examined.

714





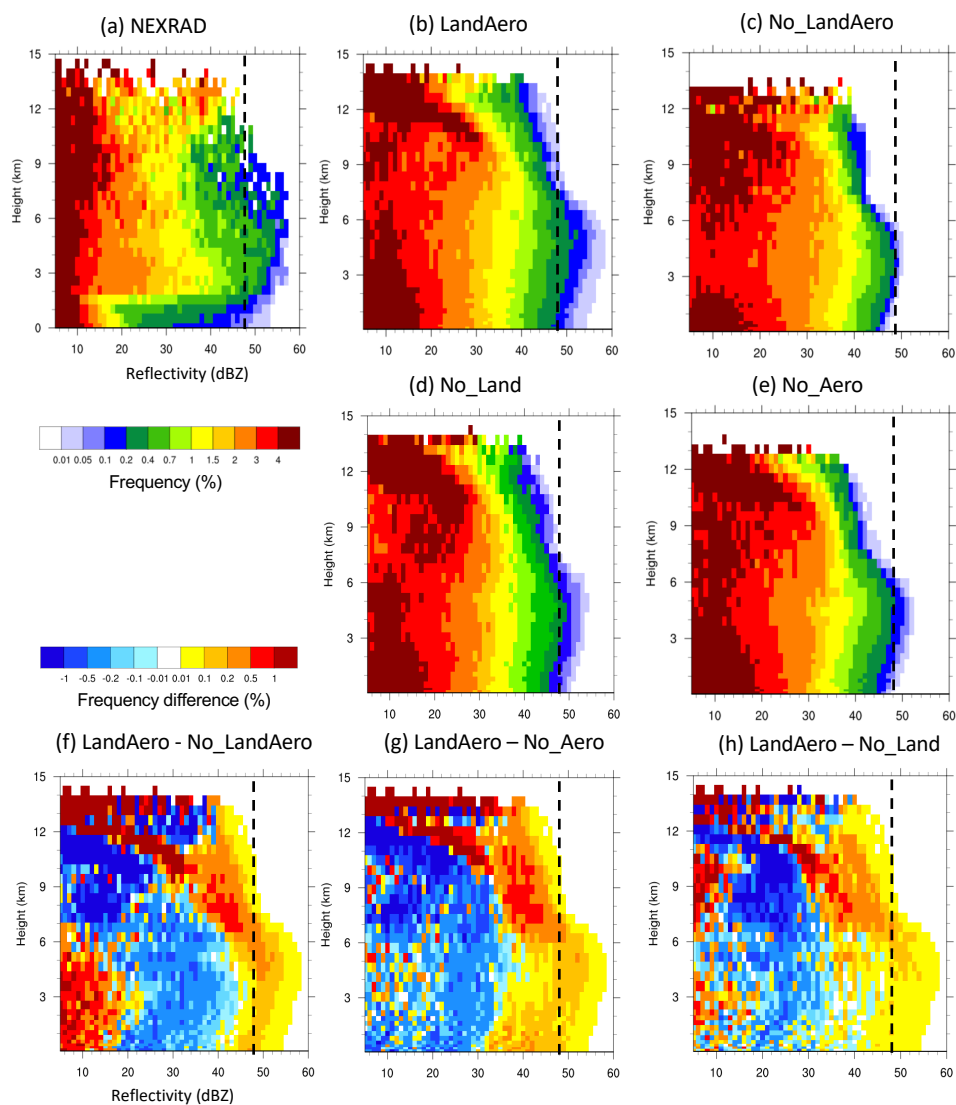
715

716 **Figure 5** Composite reflectivity (dBZ) from (a) NEXRAD (2217 UTC), (b) LandAero (2140  
717 UTC), (c) No\_LandAero (2120 UTC), (d) No\_Land (2135 UTC), and (e) No\_Aero (2125 UTC)  
718 at the time when the maximal reflectivity of the storm in Houston is reached. Houston city is  
719 marked as dark grey solid contour based on the land cover data shown in Figure 2c. The red box  
720 is the study area for the Houston convective cell.

721



722

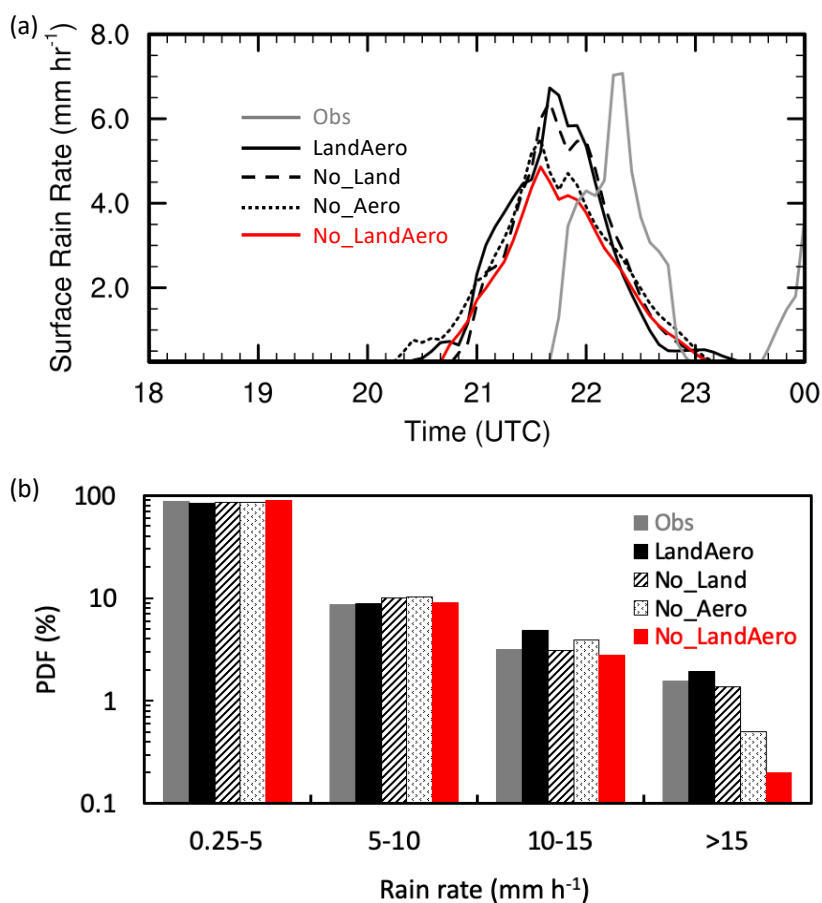


723

724 **Figure 6** Contoured frequency by altitude diagram (CFAD; %) of reflectivity for the values  
725 larger than 0 dBZ from (a) NEXRAD, (b) LandAero, (c) No\_LandAero, (d) No\_Land, and (e)  
726 No\_Aero. (f-h) present the differences of CFAD (%) of reflectivity for (f) LandAero -  
727 No\_LandAero, (g) LandAero - No\_Aero, and (h) LandAero - No\_Land. Data are from the study  
728 area (red box in Figure 5) over 1800 UTC 19 Jun to 0000 UTC 20 Jun. The vertical dashed line  
729 marks the value for reflectivity of 48 dBZ.

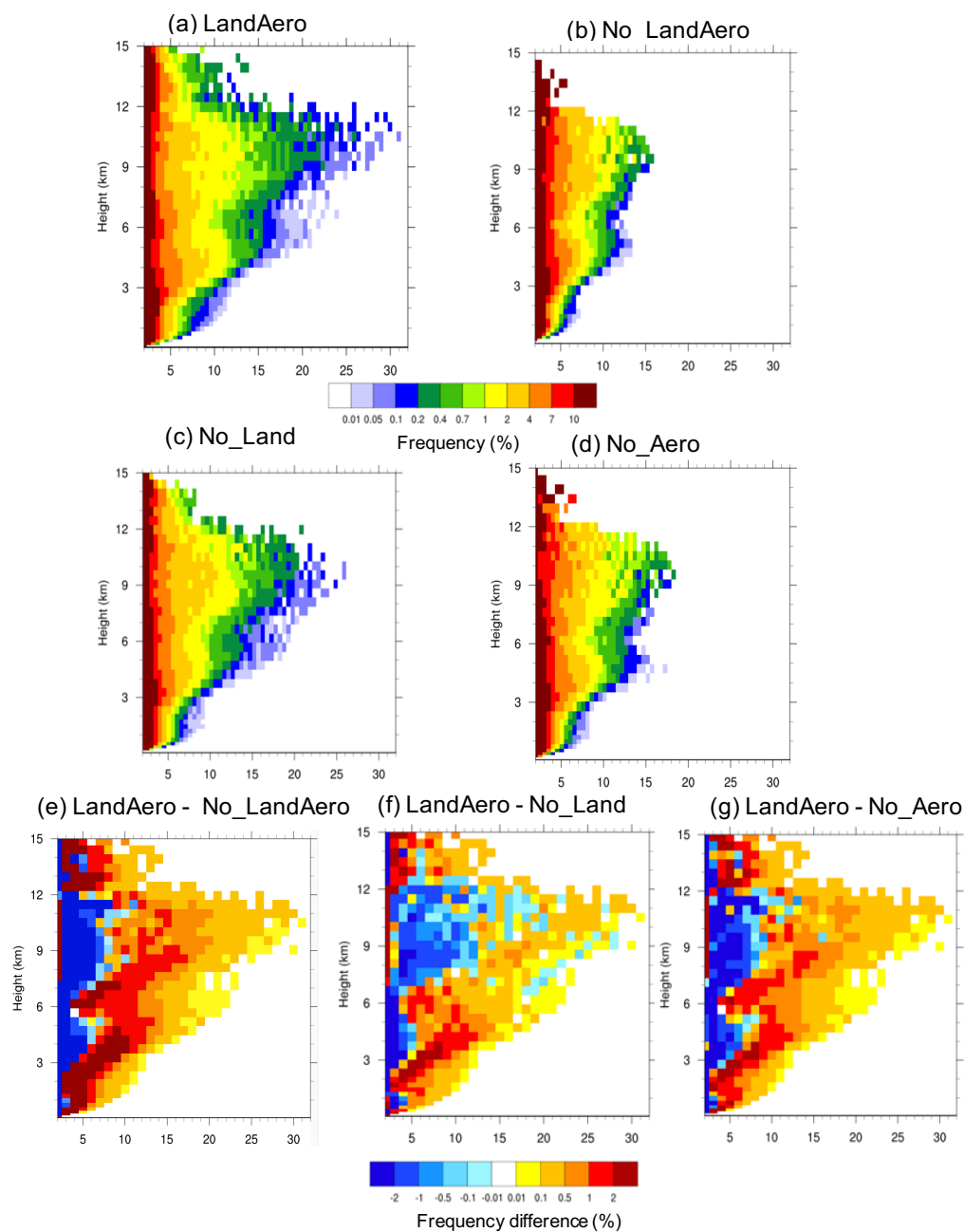


730



731

732 **Figure 7** (a) Time series of surface rain rate (mm h<sup>-1</sup>) averaged over the values larger than 0.25  
733 mm h<sup>-1</sup> for the Houston convective cell (red box in Figure 5) and (b) PDFs (%) of rain rates (>  
734 0.25 mm h<sup>-1</sup>) from 1800UTC 19 Jun to 0000 UTC 20 Jun 2013, from Observations, LandAero,  
735 No\_LandAero, No\_Land, and No\_Aero. The observation is the NEXRAD retrieved rain rate.  
736 Both observation and model data are in every 5-min frequency.

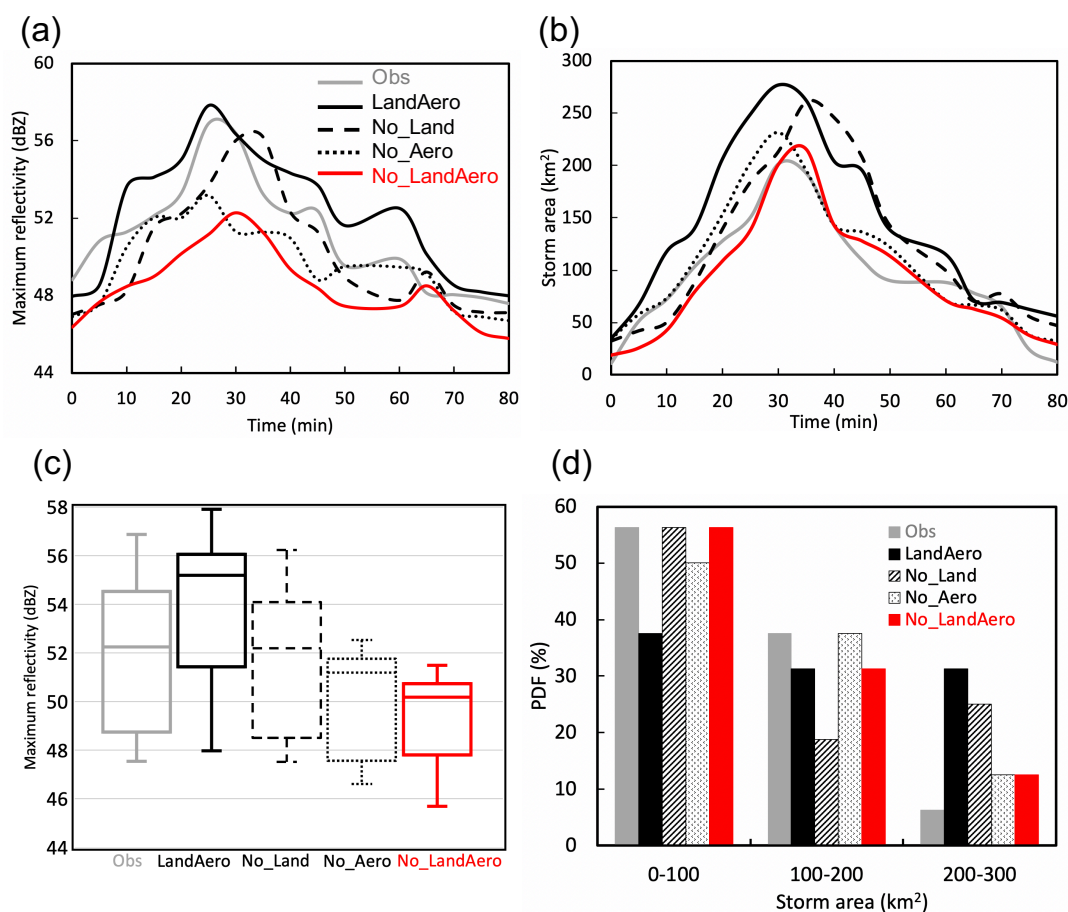


737

738 **Figure 8** CFAD (%) of updraft velocity for values larger than  $2 \text{ m s}^{-1}$  from (a) LandAero, (b)  
739 LandAero - No\_LandAero, (c) LandAero - No\_Land, and (d) LandAero - No\_Aero over the  
740 study area as shown in the red box in Figure 5 during the strong convection periods (60-min



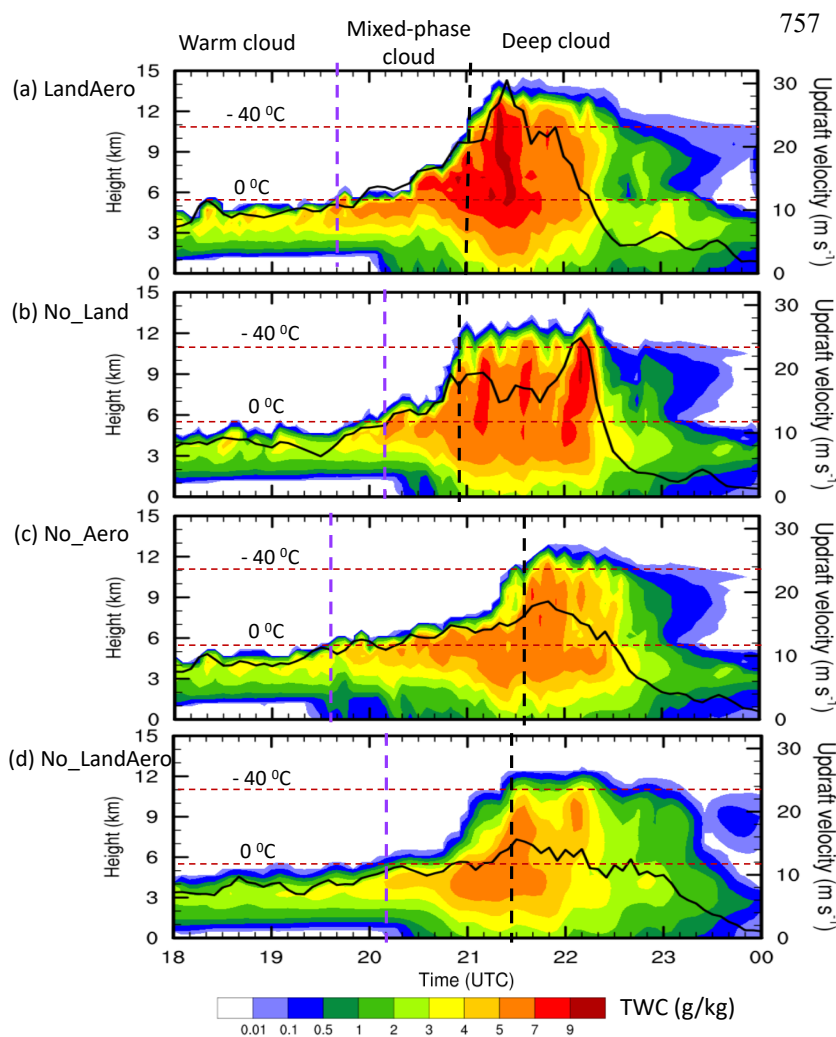
741 duration with 30 min before and after the strongest convection). (e-g) present the differences of  
 742 CFAD (%) of reflectivity for (e) LandAero - No\_LandAero, (f) LandAero -No\_Land, and (g)  
 743 LandAero – No\_Aero.  
 744



745  
 746 **Figure 9** Time series of (a) maximum reflectivity (dBZ) and (b) storm area (km<sup>2</sup>) for the tracked  
 747 convective cell from NEXRAD, LandAero, No\_LandAero, No\_Land, and No\_Aero. The time  
 748 window is from 2140 UTC to 2300 UTC for observations and from 2100 UTC to 2220 UTC for  
 749 model simulations. (c) Box-whisker plots of maximum reflectivity and (d) PDFs of averaged  
 750 storm areas for the Houston cell from NEXRAD, LandAero, No\_LandAero, No\_Land, and  
 751 No\_Aero over the respective 80 min time windows as described above. The center line of the  
 752 box indicates the median value, and the lower (upper) edge of the box indicates the 25<sup>th</sup> (75<sup>th</sup>)



753 percentiles. The whiskers indicate the minimum and maximum values. The storm area of the  
754 tracked cell is defined as the number of grid points with LWP > 50 g m<sup>-2</sup> multiplied by the grid  
755 box area (0.5 km \* 0.5 km).  
756



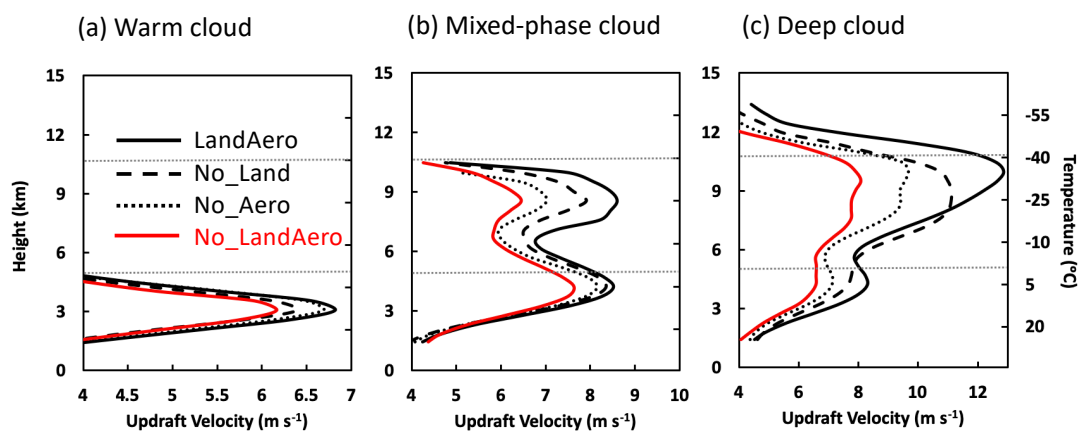
758  
759 **Figure 10** Time series of maximal total water content (shaded) and maximal updraft velocity  
760 (black line, second y-axis) over the study area as shown in the red box in Figure 5 from  
761 LandAero, No\_LandAero, No\_Land, and No\_Aero. Brown horizontal dashed lines denote the



762 freezing level (0 °C) and homogeneous freezing level (-40 °C). The initiation of mix-phase cloud  
763 and deep cloud is denoted by the purple and black vertical dashed line, respectively.  
764



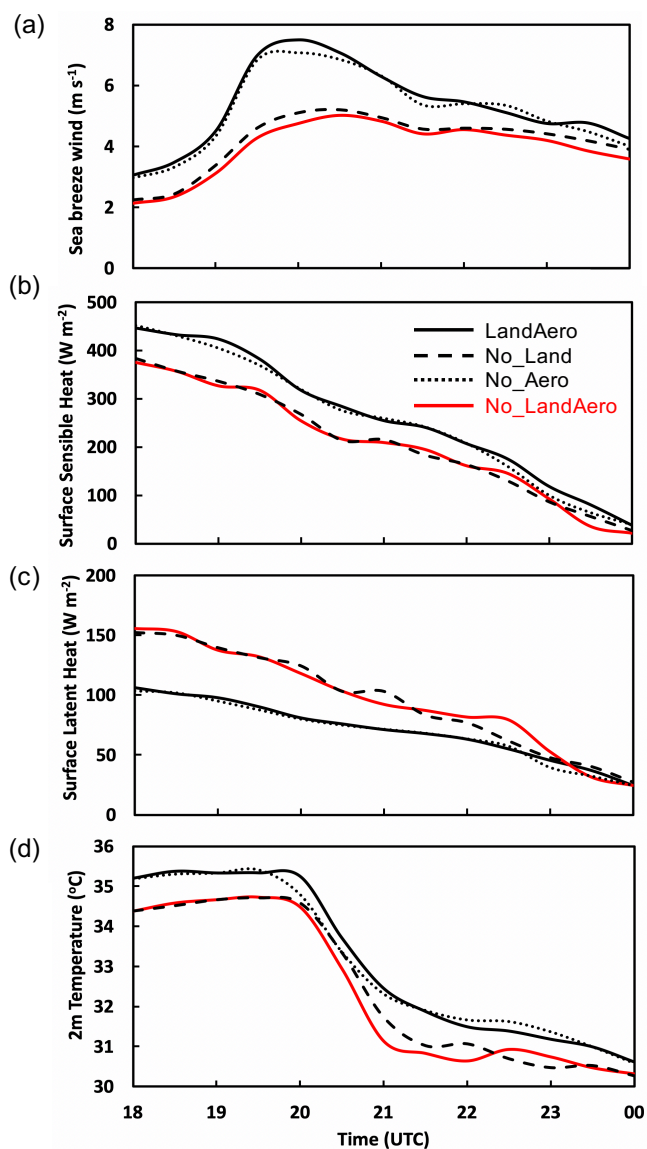
765



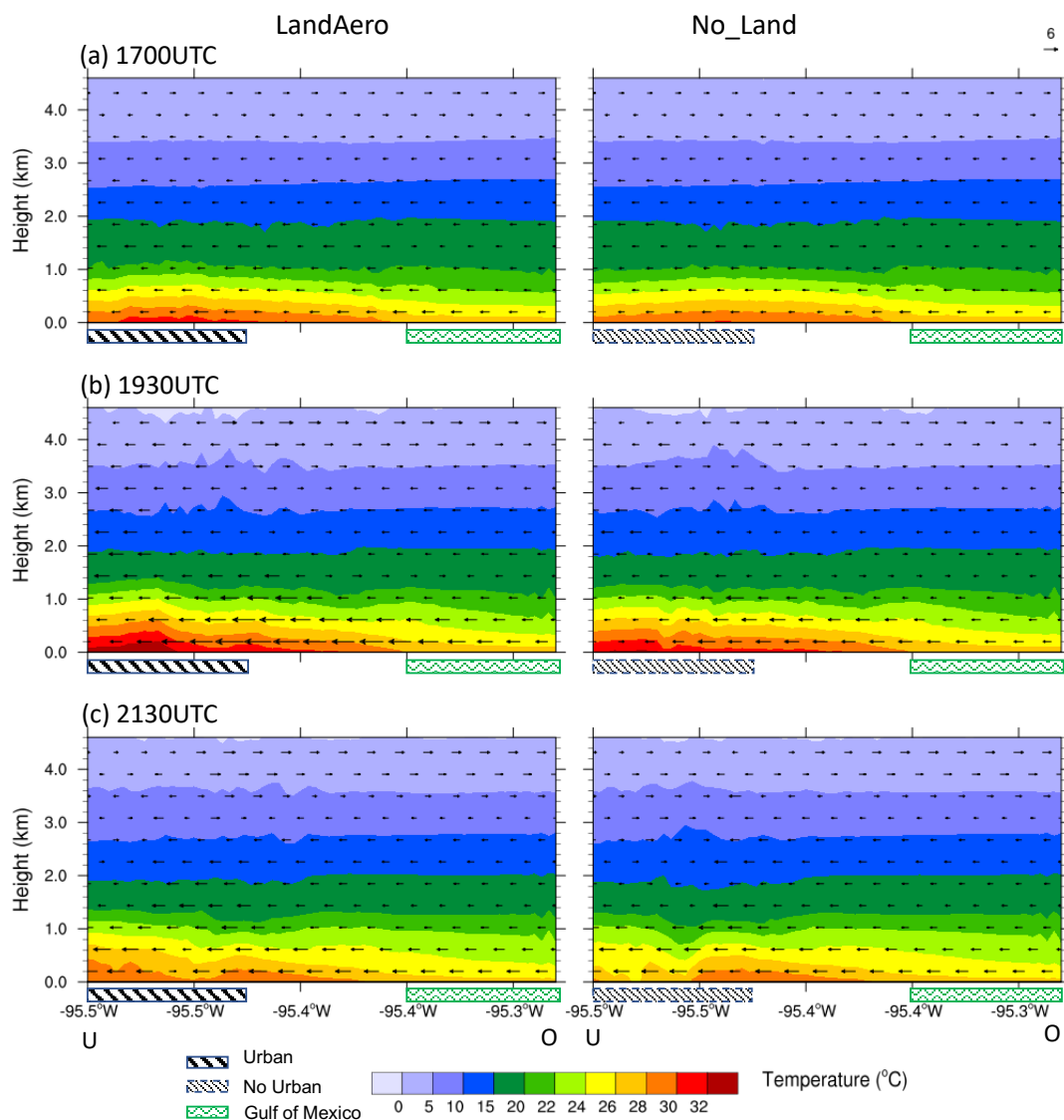
766

767 **Figure 11** Vertical profiles of updraft velocity averaged over the top 25 percentiles (i.e., 75th to  
768 100th) of the updrafts with value greater than  $2 \text{ m s}^{-1}$  from the simulations LandAero,  
769 No\_LandAero, No\_Land, and No\_Aero over the study area at the (a) warm cloud, (b) mixed-  
770 phase cloud, and (c) deep cloud stages. The dotted line denotes the freezing level ( $0 \text{ }^{\circ}\text{C}$ ).





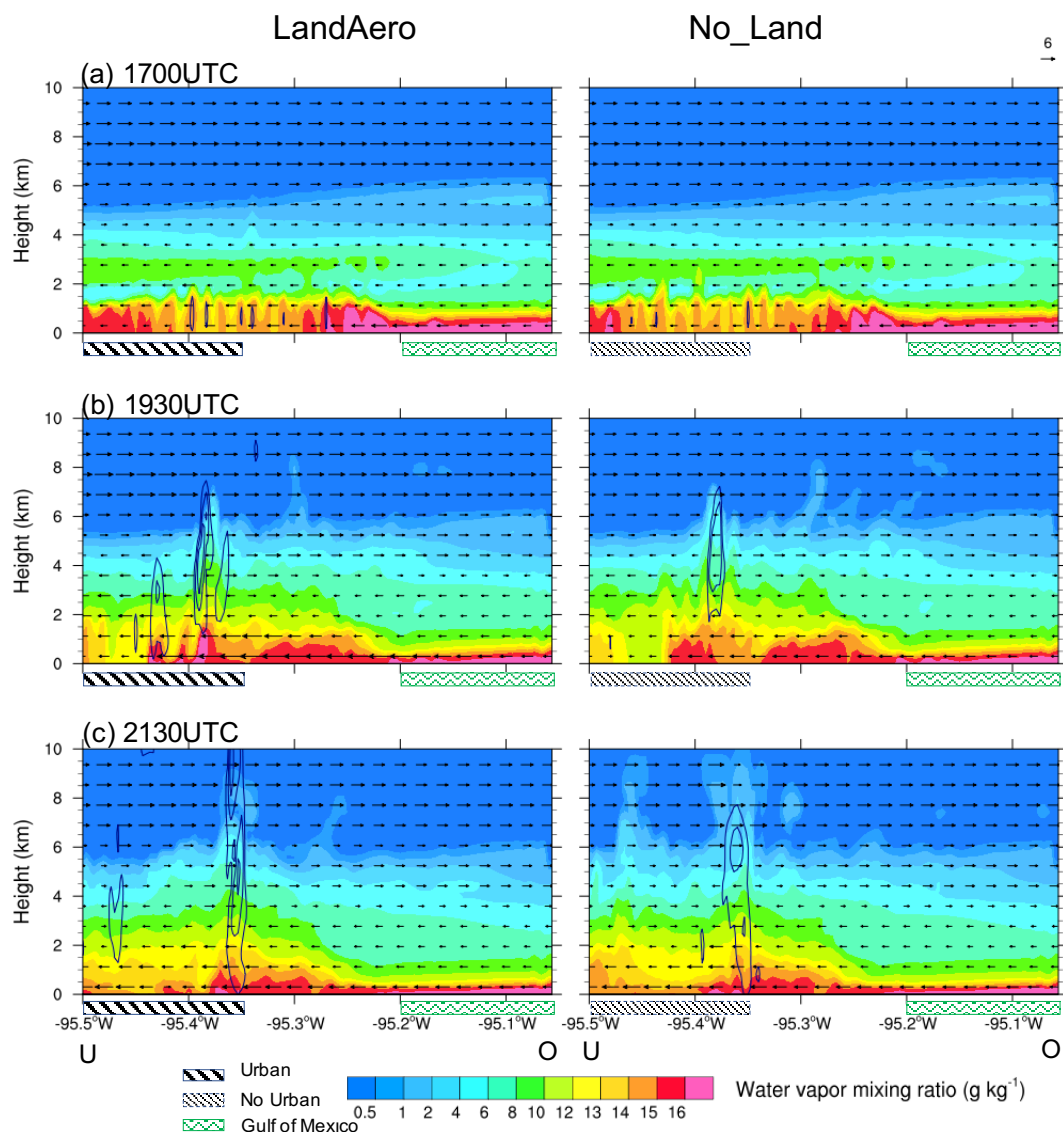
771  
772 **Figure 12** Time series of (a) sea breeze wind speed (m s<sup>-1</sup>), (b) surface sensible heat flux (W m<sup>-2</sup>), (c) surface latent heat flux (W m<sup>-2</sup>), (d) 2-m temperature (°C) from LandAero, No\_Land,  
773  
774 No\_Aero and No\_LandAero. Sea breeze winds are averaged over the horizontal winds along line  
775 UO (Figure 4a) from O to U below 1km. Heat fluxes and temperature are averaged over the  
776 study area.  
777



778

779 **Figure 13** Vertical cross sections of temperature ( $^{\circ}\text{C}$ ; shaded) and wind vectors ( $\text{m s}^{-1}$ ) along the  
 780 line UO in Figure 4a for LandAero (left) and No\_Land (right) at (a) 1700, (b) 1930, and (c) 2130  
 781 UTC. The bars with stripes and waves on the x-axis represent the urban land and water body in  
 782 Gulf of Mexico, respectively.

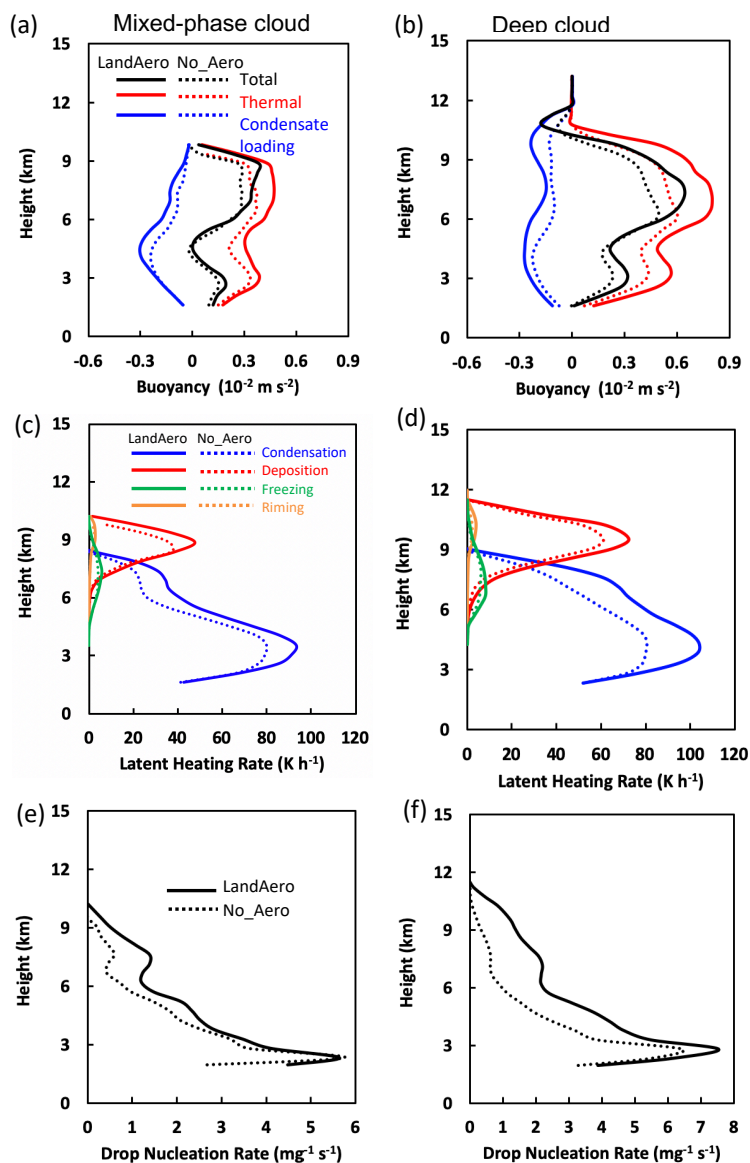
783



784

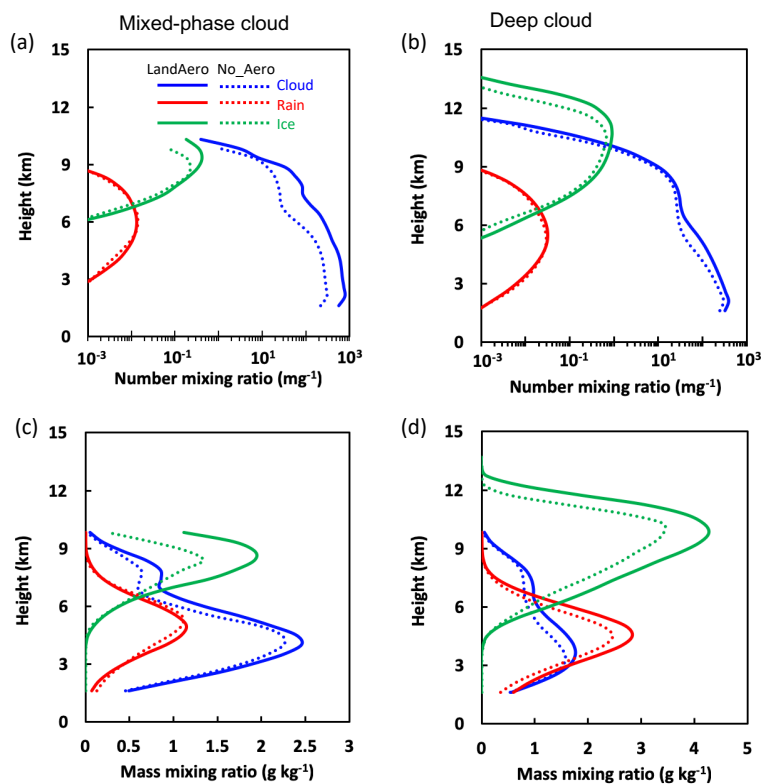
785 **Figure 14** Vertical cross sections of water vapor mixing ratio ( $\text{g kg}^{-1}$ ; shaded), updraft velocity  
786 (contour lines are 2, 6, and 11  $\text{m s}^{-1}$ ), and wind vectors along the line UO in Figure 4a for  
787 LandAero and No\_Land at (a) 1700, (b) 1930, and (c) 2130 UTC.

788



789

790 **Figure 15** Vertical profiles of (a-b) buoyancy terms ( $\text{m s}^{-2}$ ; red for Thermal buoyancy, blue for  
 791 condensate loading and black for total buoyancy), (c-d) latent heating ( $\text{K h}^{-1}$ ) from condensation  
 792 (blue), deposition (red), drop freezing (orange), and riming (green), and (e-f) droplet nucleation  
 793 rate ( $\text{mg}^{-1} \text{ s}^{-1}$ ) averaged over the top 25 percentiles (i.e., 75th to 100th) of the updrafts with value  
 794 greater than  $2 \text{ m s}^{-1}$  from the simulations LandAero and No\_Aero in the study area during the  
 795 mixed-phase cloud (left) and deep cloud (right) stages.



796

797 **Figure 16** Vertical profiles of (a-b) number mixing ratio ( $\text{mg}^{-1}$ ) and (c-d) mass mixing ratio ( $\text{g}$   
798  $\text{kg}^{-1}$ ) of cloud droplets (blue), rain drops (red) and ice particles (green) averaged over the top 25  
799 percentiles (i.e., 75th to 100th) of the updrafts with value greater than  $2 \text{ m s}^{-1}$  from the  
800 simulations LandAero and No\_Aero in the study area during the mixed-phase cloud (left) and  
801 deep cloud (right) stages.